AFRL-RH-FS-TR-2023-0005

Flexible Broadband Optical Device

Edward A. Pier
Oceanit

Wei-Chuan Shih
Mohsen Rakhshandehroo
University of Houston

Joel N. Bixler
711th Human Performance Wing
Airman Systems Directorate
Bioeffects Division
Optical Radiation Bioeffects Branch

March 2023

Final Report - Dec 2019 to Mar 2023

Air Force Research Laboratory 711th Human Performance Wing Airman Systems Directorate Bioeffects Division Optical Radiation Bioeffects Branch JBSA Fort Sam Houston, Texas 78234

NOTICE AND SIGNATURE PAGE

Using Government drawings, specifications, or other data included in this document for any purpose other than Government procurement does not in any way obligate the U.S. Government. The fact that the Government formulated or supplied the drawings, specifications, or other data does not license the holder or any other person or corporations; or convey any rights or permission to manufacture, use, or sell any patented invention that may relate to them.

This report was cleared for public release by the AFRL Public Affairs Office and is available to the general public, including foreign nationals. Copies may be obtained from the Defense Technical Information Center (DTIC) (http://www.dtic.mil).

"Flexible Broadband Optical Device"

(AFRL-RH-FS-TR- 2023- 0005) has been reviewed and is approved for publication in accordance with assigned distribution statement.

FERRIS.LYNDSEY.MARIE.1381070391 Digitally signed by FERRIS.LYNDSEY.MARIE.1381070391 Date: 2023.03.21 12:41:01 -05'00'

LYNDSEY M. FERRIS, LtCol, USAF, BSC
Chief, Optical Radiation Bioeffects Branch

MILLER.STEPHANIE.A.1230536283 Digitally signed by MILLER.STEPHANIE.A.1230536283 Date: 2023.04.18 13:03:19 -05'00'

STEPHANIE A. MILLER, DR-IV, DAF
Chief, Bioeffects Division
Airman Systems Directorate
711th Human Performance Wing
Air Force Research Laboratory

This report is published in the interest of scientific and technical information exchange, and its publication does not constitute an official position of the U.S. Government.

REPORT DOCUMENTATION PAGE

Form Approved
OMB No. 0704–0188

1. REPORT DATE *(DD–MM–YYYY)*	2. REPORT TYPE	3. DATES COVERED *(From — To)*
03-01-2023	Final Technical Report	Dec 2019 to Mar 2023

4. TITLE AND SUBTITLE

Flexible Broadband Optical Device

5a. CONTRACT NUMBER
FA8650-19-C-6988

5b. GRANT NUMBER

5c. PROGRAM ELEMENT NUMBER

6. AUTHOR(S)

Edward A. Pier, Wei-Chuan Shih, Mohsen Rakhshandehroo, Joel N. Bixler

5d. PROJECT NUMBER

5e. TASK NUMBER

5f. WORK UNIT NUMBER
H0WS

7. PERFORMING ORGANIZATION NAME(S) AND ADDRESS(ES)
Oceanit
828 Fort Street Mall
Suite 600
Honolulu, HI 96813

8. PERFORMING ORGANIZATION REPORT NUMBER

9. SPONSORING / MONITORING AGENCY NAME(S) AND ADDRESS(ES)
Air Force Research Laboratory
711th Human Performance Wing
Airman Systems Directorate
Bioeffects Division
Optical Radiation Bioeffects Branch

10. SPONSOR/MONITOR'S ACRONYM(S)
711 HPW/RHDO

11. SPONSOR/MONITOR'S REPORT NUMBER(S)
AFRL-RH-FS-TR-2023-0005

12. DISTRIBUTION / AVAILABILITY STATEMENT
DISTRIBUTION STATEMENT A. Distribution for public release; distribution in unlimited. CLEARED: PA Case # AFRL-2023-0445. The views expressed are those of the author and do not necessarily reflect the official policy or position of the Department of the Air Force, the Department of

13. SUPPLEMENTARY NOTES
Defense, or the U.S government.

14. ABSTRACT

This project had two components. For the first component, Oceanit and The University of Houston built a prototype device for measuring the optical properties of a sample. The device illuminates the sample and measures the angular distribution of light scattered from and transmitted through it. We then analyze these measurements using a neural net to derive the sample's optical properties. For the first component, we modeled time-dependent radiative transfer through a sample, in order to support ultra-high-speed imaging efforts at RHDO.

15. SUBJECT TERMS

Optical Properties Radiative Transfer

16. SECURITY CLASSIFICATION OF:			17. LIMITATION OF ABSTRACT	18. NUMBER OF PAGES	19a. NAME OF RESPONSIBLE PERSON
a. REPORT	b. ABSTRACT	c. THIS PAGE			Joel N. Bixler
U	U	U	U	45	19b. TELEPHONE NUMBER *(include area code)* 210-539-8172

This Page Intentionally Left Blank

TABLE OF CONTENTS

LIST OF FIGURES

LIST OF TABLES

1.0 INTRODUCTION

The way a material interacts with light reveals a wealth of information about its composition and structure. This principle forms the basis of entire fields, such as astronomy and remote sensing. In biology, it allows non-invasive and non-destructive measurements of tissue that can be crucial for investigating life processes and measuring the states of disease and injury. A flexible, low cost instrument capable of measuring absorption and scattering parameters would have a significant impact on a number of fields, but no such device currently exists. Moreover, the computational framework for deriving intrinsic optical properties from measurements is currently not well developed.

This report describes the development and optimization of a device capable of measuring the optical properties of samples. This device illuminates a sample and measures the angular distribution of light scattered from and transmitted through it. We then apply a neural net trained on radiative transfer models to derive the optical properties.

A second component of this project was an effort to model the time-dependent propagation of light through a sample. The advent of femtosecond imaging using T-CUP cameras (Liang and Wang, 2018) makes it possible for the first time to directly observe such propagation in the laboratory. Previously, time dependent propagation of light was solely of interest to astronomers.

2.0 THE DEVICE

2.1 Introduction

The ability of light to penetrate human tissue, interrogate its components, and escape it, is a key factor in diagnostic applications of tissues (Farrell, Patterson, and Wilson, 1992, Pfaff et al., 2015, Lanzafame et al., 2014). Therefore, optical properties of human tissue have been studied both analytically and numerically by many researchers (Mignon et al., 2018). These properties are mainly reflected by coefficients such as absorption coefficient, μ_a (mm^{-1}), scattering coefficient μ_s (mm^{-1}), anisotropy g, and reduced scattering coefficient, μ_s' (mm^{-1}). Numerous articles have measured such optical properties for different skin layers and reported a wide variation of absorption and scattering properties (DeLisi et al., 2019, Simpson et al., 1998, Salomatina et al., 2006, Bashkatov et al., 2005, Mignon et al., 2018, Wang, Jacques, and Zheng, 1995). Precise reflectance/transmittance measurements are usually employed to assess these optical properties. Such measurements and analyses are generally performed using integrating sphere methods (Edwards et al., 1961, Jacquez and Kuppenheim, 1955, Würth and Resch-Genger, 2015, Dam et al., 2000, Friebel et al., 2006, Pickering et al., 1992, Roggan et al., 1994) which lack angular resolution. Alternatively, optical fibers have been employed on rotational goniometers (Li et al., 2006, Baribeau, Neil, and Cote, 2009, Ferrero et al., 2013, Schröder et al., 2011) to provide angle-resolved reflectance of the specimen. Rotational movements, however, require a highly precise mechanical design and are time-consuming. Even though it is possible to employ multiple detectors to reduce data acquisition time, moving parts inher-

ently necessitate regular maintenance and calibration to guarantee reproducibility. Early employment of multi-detector goniometric measurements utilized an arc of fiber optic receivers surrounding the specimen (Vorburger et al., 1984).

To address the aforementioned issue, fixed position camera detectors have been employed for diffuse reflectance measurements. Jacques, 1993 used a fixed video camera to measure radial diffuse reflection of tissue samples. Sole, Farup, and Tominaga, 2015 used an NIR camera to measure spatial diffuse reflectance of Fuji apples. Ma et al., 2018 used a digital camera to measure spatially resolved diffuse reflectance of flexible objects at different incident angles. Using a single camera in these measurements improved the acquisition time but limited the spatial range of detection to the sensor size of the camera. In order to improve the detection range, one may employ a multiple-camera detection system, where multiple stationary cameras are utilized to measure angle-resolved reflectance from biological tissue samples.

As an alternative to experimental measurements, the diffuse reflectance profile has been studied by Kienle et al., 1996, and later by Qu, Huang, and J., 2000 using Monte Carlo simulations. They found that the angle-resolved diffuse reflectance profile is in close agreement with Lambertian distribution. Xia and Yao, 2007 measured the diffuse reflectance angular distribution in biological tissues under different incident angles and found a nearly Lambertian distribution for normal incidence. Therefore, many researchers use Lambertian distribution as the calibration baseline for their experimental measurements.

In this paper, a system is introduced for Angular Reflectance and Transmittence (ART) profile measurements with multiple stationary cameras. Using multiple compact, large pixel-count CMOS cameras, the measuring system covers a large angular reflection range (52°) with fine angular resolution (0.02° per pixel). To validate the results, ART profile of tissue phantoms with different optical properties were measured. As an application example, ART profiles were measured for porcine dermis and subcutaneous fat which are a model for human skin in terms of structure (Debeer et al., 2013, Eggleston et al., 2000,Vincelette et al., 2012,). Monte Carlo (MC) simulations were used to generate ART profiles from a set of tissue optical properties. Absorption and reduced scattering coefficients were obtained by calculating the minimum root mean square error difference between the experimentally measured ART and MC-generated results. Additionally, machine learning method was used to extract optical properties using ART profiles. Random forest (RF) classifier was trained using the MC-generated look-up table as the input. To validate the extracted optical properties, the conventional method of integrating sphere (IS) was employed. Based on the measured signal split by IS, optical properties were calculated using inverse adding doubling (IAD) program (Prahl, Gemert, and Welch, 1993) and were considered as the ground truth.

2.2 Materials and Methods

2.2.1 Experimental Setup

As shown in Figure 1, the experimental setup for reflection measurements consists of three fixed position sCMOS cameras (Quantalux, Thorlabs), thereby eliminating any moving part and its associated hinders. A 633 nm HeNe CW laser is irradiated on the specimen mounted on a sample stage normal to the incident laser light. Angle resolved reflectance (ARR) is acquired by the cameras, each having a relay lens (L1, L2, L3 in Figure 1b) of 40 mm focal length. The first camera (C1) covers 14.2° to 31.4°, the second camera (C2) 37.3° to 54.6°, and the third camera (C3) 60.1° to 77.5° with respect to surface normal. Transmission measurements are carried by a single camera (C4) placed right after the sample, with 13mm distance from the sensor which covers $-20°$ to $+20°$ of the transmitted signal. A transmissive diffuser (Thorlabs- DG10-120) is placed after the laser source to reduce coherence and speckles. The diffuser causes some beam divergence, and hence, a double iris setup has been used to produce a 2-mm spot on the sample (see Figure 1).

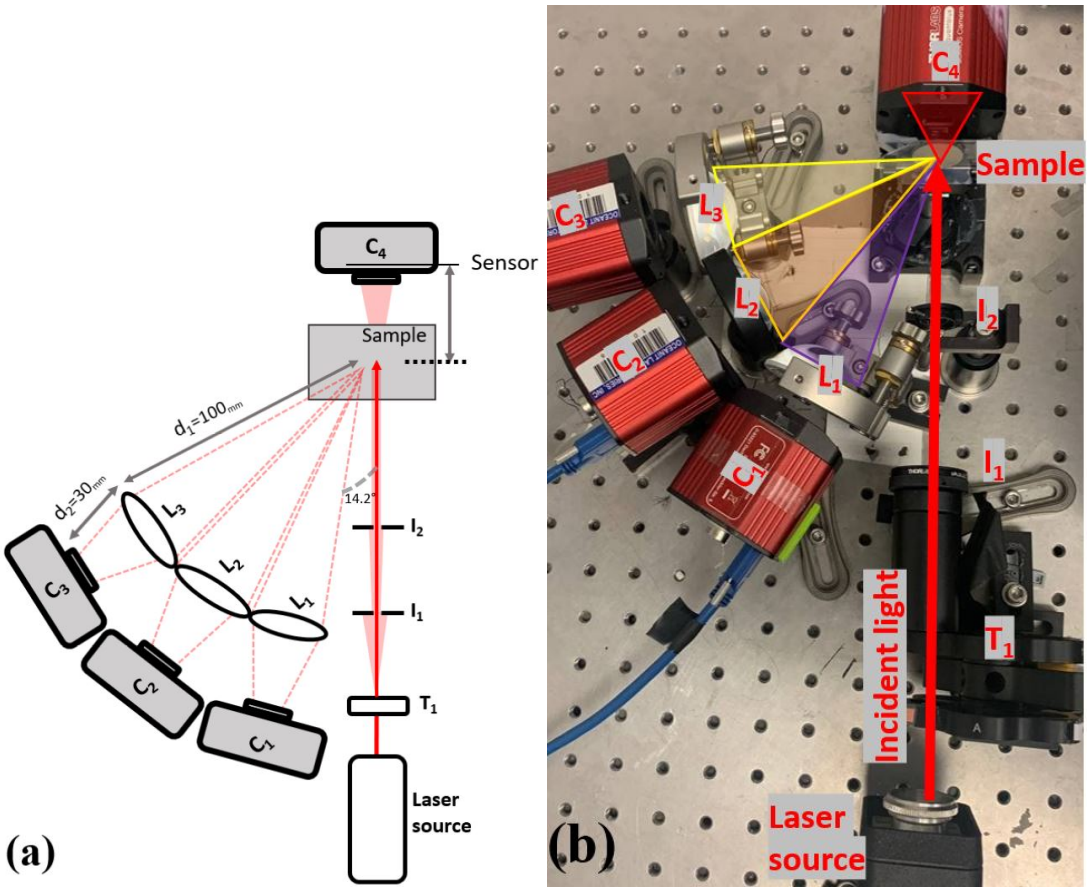

Figure 1. Top view of the experimental setup: (a) design schematic and (b) physical setup

2.2.2 Data Acquisition and Monte Carlo Models

The diffuse reflected light captured by the three 1920x1080 cameras is binned over the central 300 pixels vertically, where the curvature effect of the relaying lens is negligible. The acquired profile is then translated to an ARR profile by the calibration procedure explained in section 2.4. The calibration process is then validated by measuring ARR profile of three phantoms with different optical properties and comparing them with their respective MC generated ARR profiles. The transmitted light captured by C_4 camera is binned over the entire 1080 vertical pixels and plotted against the horizontal pixels.

The MC technique used to simulate ART profiles is based on numerical simulations of photon transport in a scattering media developed by Wang, Jacques, and Zheng, 1995. The model utilizes three parameters to model scattering events: absorption coefficient (μ_a), reduced scattering coefficient (μ_s'), and scattering phase function g . In this study, a Henyey-Greenstein scattering phase function has been used with an average cosine of $g = 0.9$ (Beek et al., 1997) and 5 million photons for each simulation. Probability of photons exiting the sample at the boundaries depends on whether the incidence angle at the tissue-air interface exceeds the critical angle for total internal reflection. If the photon is determined to exit, the exit angle is calculated by Snell's law.

The ART look up table was generated using MC simulations with respect to various tissue optical properties. Refractive indices for dermis and fat were assumed to be $n_{\text{dermis}} = 1.4$ and $n_{\text{fat}} = 1.44$, respectively (Bolin et al., 1989). The modeled tissue had the same dimensions as the measured samples: a 1.2 mm thickness, a 2 mm full width half maximum (FWHM), Gaussian beam incident at normal, and laterally infinite. Absorption and reduced scattering coefficients were obtained by scanning for the minimum root mean square error (RMSE) difference between the experimentally collected ART profile, and MC generated results.

To validate the extracted optical properties, the conventional method of integrating sphere was employed. Utilizing a single-integrating sphere accessory, total reflectance and total transmittance of tissue samples were measured. Based on the measured signal split, the reduced scattering coefficient μ_s' and absorption coefficient μ_a were calculated using inverse adding-doubling (IAD) program developed by Prahl, Gemert, and Welch, 1993. The program operates by repeatedly guessing the optical properties and comparing the expected measurements with those that the researcher has made. The "doubling" method assumes that the reflected and transmitted light is known for one thin layer. Then the contributions of a slab that is twice as thick is found by adding two identical slabs until the desired thickness is reached. The "adding" method extends the doubling method to dissimilar slabs which is out of scope of this paper.

Table 1. Optical properties of phantom samples

Phantom	μ_a	μ_s'
Phantom 1 (scattering only)	0.0 (no ink)	$2.98\,\mathrm{mm}^{-1}$
Phantom 2 (near dermis)	$0.042\,\mathrm{mm}^{-1}$	$2.98\,\mathrm{mm}^{-1}$
Phantom 3 (near fat)	$0.042\,\mathrm{mm}^{-1}$	$1.12\,\mathrm{mm}^{-1}$

2.2.3 Tissue phantoms using polystyrene beads and India Ink

Performance of the ART detection system was first evaluated with tissue phantom measurements. Tissue phantoms were produced using polystyrene beads (PSBs) (Polysciences; Warrington, PA) suspended in water ($n = 1.33$) as the scattering component. Reduced scattering coefficient of the phantoms was calculated using a Mie theory-based MATLAB program developed by Scott Prahl[1]. Reduced scattering coefficient (μ_s') was varied by altering the volume fraction of 1.93 μm diameter PSBs with $n = 1.57$ at 633nm. Absorption coefficient (μ_a) was introduced to the phantoms by using diluted black India ink (Super Black India Ink, Speedball) which possesses a nearly flat absorption profile around 633nm. Three phantoms were made: phantom 1 with $\mu_s' = 2.98\,\mathrm{mm}^{-1}$ and $\mu_a = 0\,\mathrm{mm}^{-1}$ (no ink), phantom 2 with $\mu_s' = 2.98\,\mathrm{mm}^{-1}$ $\mu_a = 0.042\,\mathrm{mm}^{-1}$, and phantom 3 with $\mu_s' = 1.12\,\mathrm{mm}^{-1}$ and $\mu_a = 0.042\,\mathrm{mm}^{-1}$. For the phantom measurements, a cuvette with 1 mm pathlength and 1.2 mm thick glass walls was used. The same physical properties were used in MC simulations.

For the real tissue measurements, porcine dermis and subcutaneous fat extracted from Yucatan minipig skin were used. It has been proven that Yucatan minipig has many similarities with human skin in terms of pigment content, structure and immunochemistry (Debeer et al., 2013, Eggleston et al., 2000, Vincelette et al., 2012). Tissue samples maintained a 1.2 ± 0.1 mm thickness and a 1.5 cm diameter. Samples were stored in -20° C freezer and defrosted prior to the experiments. To place tissue samples on the sample holder, they were sandwiched between two no. 1 coverslips (0.15 mm thick).

2.2.4 Angle-Resolved Reflectance (ARR) measurements

In order to assign each pixel from each camera to its respective angle of reflection, a three-step calibration procedure was developed: pixel-to-angle calibration, angular compression correction, and camera gain adjustment. A flowchart for the calibration procedure is shown in Figure 2. As shown, an optimization loop was employed for angular compression correction.

2.2.4.1 Pixel-to-angle calibration. For pixel-to-angle calibration, a 75 grooves/mm diffraction grating was used. According to the grating equation, each detected diffraction order was assigned to its corresponding angle of reflection. The equivalent angular

[1] https://omlc.org/software/mie

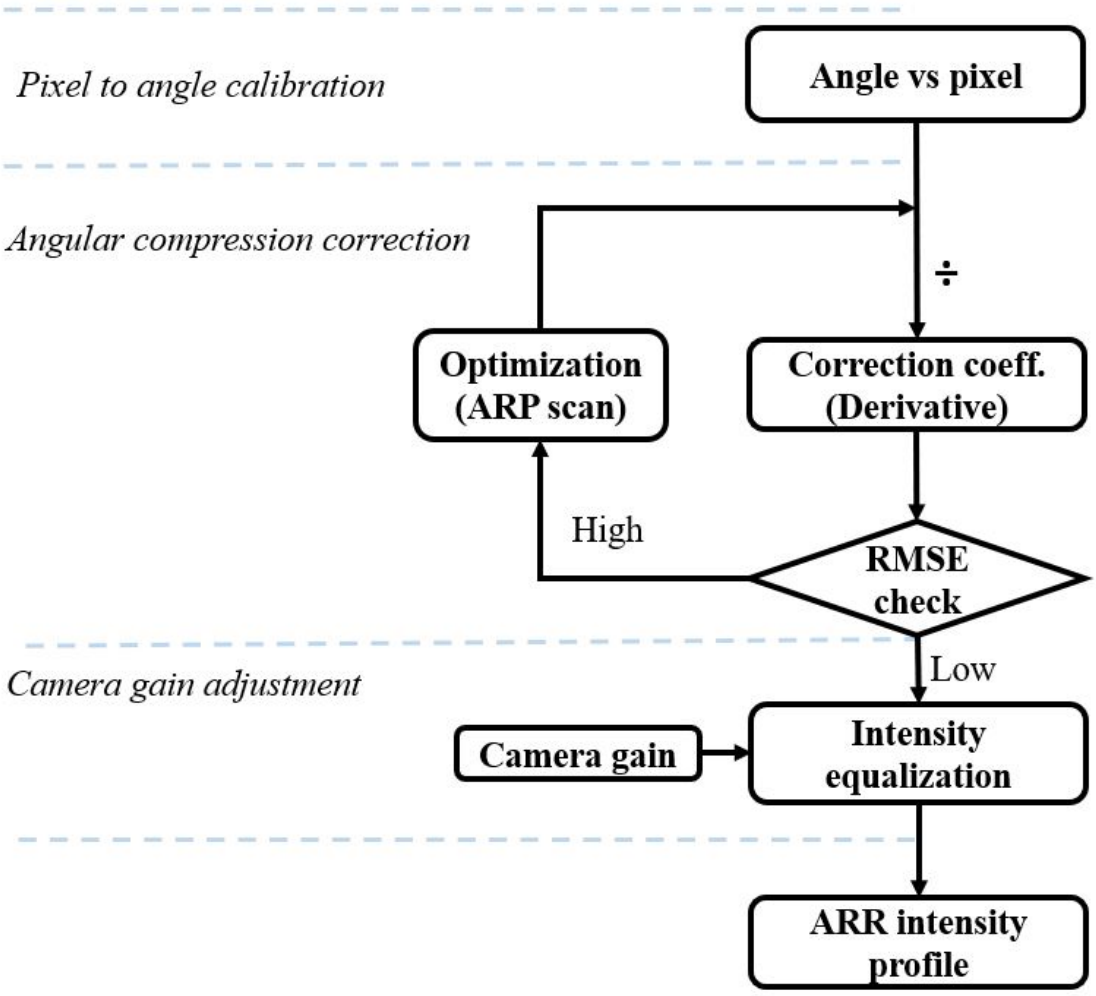

Figure 2. Flowchart for the calibration procedure of ARR intensity profile detection.

resolution for a single pixel was measured to be very small (0.02° per pixel). But the effective angular resolution, which is limited by the laser spot size, was measured to be 0.5°. By plotting the translated angle of reflection with respect to the corresponding pixel, an angle vs. pixel curve was obtained for each camera (see Figure 3a). As observed, the central pixels (pixels 700-1300) showed a constant slope on the curve, while near edge pixels showed an increase in the angle vs. pixel slope. This nonlinear behavior indicates angular compression happening on the cameras due to barrel distortion effects caused by the relay lens (Swarnakar et al., 1997, Jeught, Buytaert, and Dirckx, 2012). However, the slope of angle vs. pixel curve being almost constant for the central pixels, suggests that no angular compression happening, and such pixels may be excluded from the angular compression correction procedure.

2.2.4.2 Angular compression correction. The angular compression effect was captured by a correction coefficient obtained from the derivative of the angle vs. pixel curve in Figure 3a. This derivative was normalized with respect to the relatively constant derivative of central pixels to minimize the effect of the correction coefficient on central pixels (Figure 3b). With this normalization, the correction coefficient remained almost constant and equal to 1.0 ($\pm$0.05) for pixels in the range of 600 to 1300 (Figure 3b). Dividing the raw intensity profile by the correction coefficient, the compression artifacts were significantly reduced.

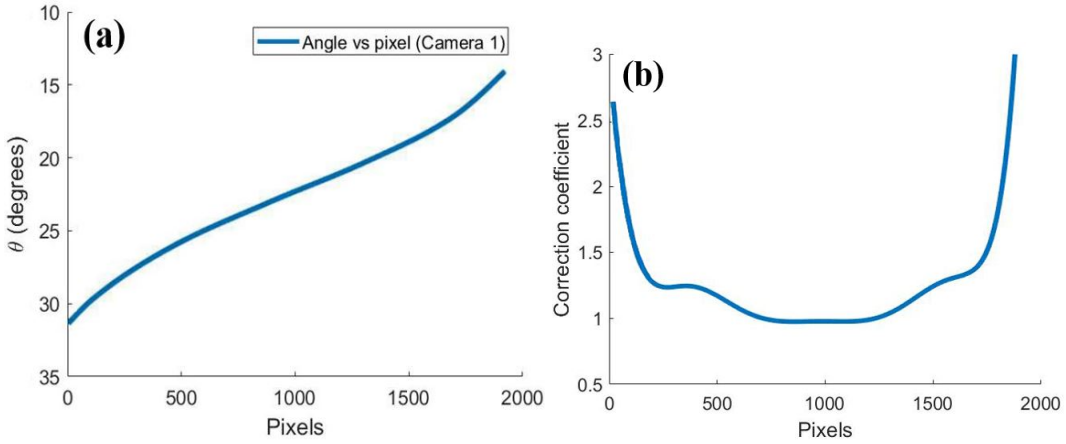

Figure 3. Camera 1's (a) angle vs pixel curve (b) correction coefficients derived from the normalized slope of angle vs. pixel curve.

An optimization process was employed to improve the correction coefficients, especially for the pixels near camera edge. This process introduced artificial reflection points (ARPs) and scanned them over the near-edge pixels at either end of the camera. An iterative two-dimensional scan was employed where one dimension scanned ARP over the 500 near edge pixels, and the second one scanned over different angles of reflection. The reflecting angles for ARPs were chosen to scan between the diffraction orders detected by the diffraction grating. For each iteration a new correction coefficient was calculated and used to correct the acquired raw intensity profile of phantom 1 . ARR profiles for tissue samples and phantoms are known to maintain a Lambertian distribution (Kienle et al., 1996). Therefore, corrected ARR profile resulting from each iteration was compared to Lambertian ARR, and the best match was obtained by minimizing the root mean squared error (RMSE) (Figure 4a).

2.2.4.3 Camera gain adjustment. Because the ARR intensity decreases when the reflection angle increases, the 3 cameras operate at different intensity levels. A gain equalization protocol is needed. An acquisition gain was assigned to each camera and utilized to make the output results continuous across cameras. Gain adjustment was performed by dividing the acquired intensity profile of each camera by its acquisition gain. Acquisition gains of 1.4 and 1.9 were used for cameras 2 and 3, respectively, while no gain adjustment

was introduced to camera 1. These gains were proven to stay the same as the measuring samples changed.

Once the calibration procedure has been implemented, the profiles were binned over 3° angular bins (Figure 4b). Phantom ARR measurements produced matching results ($< 8\%$ deviation) with MC simulated ARR profiles of the same μ_a and μ_s' when normalized with respect to the maximum intensity of phantom 1, validating the effectiveness of the calibration procedure. (Figure 4c)

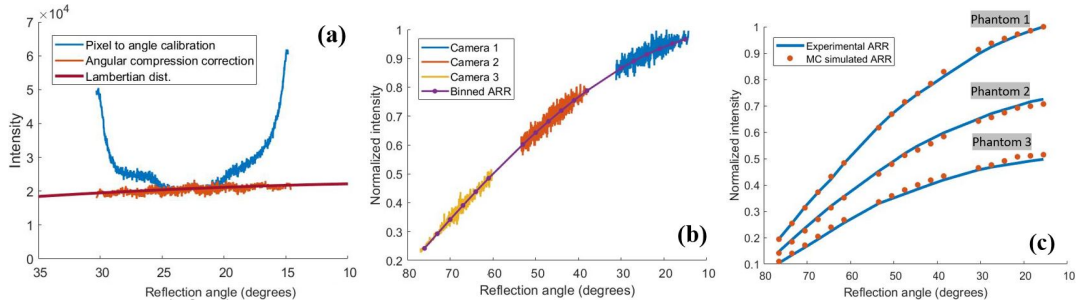

Figure 4. (a) Pixel-to-angle calibration and angular compression correction of phantom 1 for camera 1, (b) All calibrated camera acquisitions along with ARR profiles binned over 3°, (c) ARR profiles of phantom 1, 2, and 3 along with those obtained from Monte Carlo simulations.

2.2.5 Transmission profile measurements

Transmission measurements were calibrated by translating the spatially resolved profile to angle resolved. Dividing the spatial distance captured with C_4 by the sample-to-sensor distance and solving for the transmitted angle, provided the angle resolved transmission profile. Experimental angle resolved transmission profiles of phantom 2 and 3 are plotted in Figure 5 showing $< 7\%$ difference comparing to MC generated profiles with optical properties shown in Table 1. Since phantom 1 only has scattering components, its transmitted profile was not included. Profiles shown in Figure 5 are normalized with respect to maximum intensity of phantom 3.

2.2.6 Machine learning method

Random forest (RF) algorithm was used as a machine learning method to extract optical properties. RF was trained using 1400 MC generated ART profiles with μ_a and μ_s' as the input. In order to evaluate the accuracy in optical properties detection of the RF system, 80% of the input data was used for training and 20% for testing the predicted results. Figures 6a and 6b show the predicted vs true values of absorption coefficient and reduced scattering coefficient. The R^2 values and the slope of the corresponding linear fit (red line) for both figures are very close to 1, showing a high accuracy of prediction when using RF classifier.

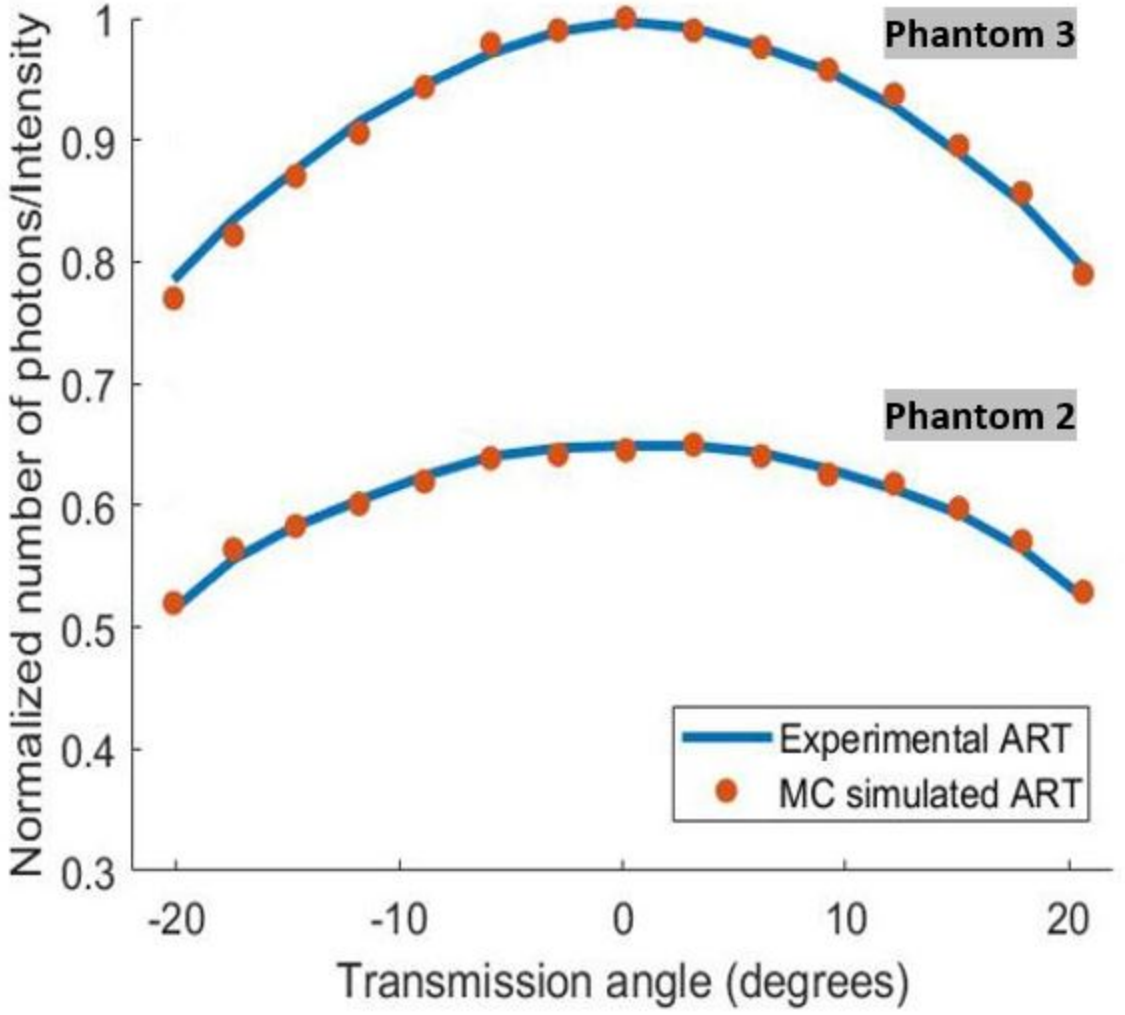

Figure 5. Angle resolved transmission profiles of phantom 2, and 3 along with those obtained from Monte Carlo simulations.

2.3 Results

2.3.1 Dermis

The ART profiles for four dermis samples were experimentally measured using our stationary system. Each experimental measurement was scanned by MC-ART method for extraction of optical properties. The ART profiles were binned over 3°, this way MC-ART showed a higher signal-to-noise ratio (SNR) than the experimentally detected ART. The MC-ART scan was implemented by calculating the RMSE difference between experimental ART measurements and the MC look-up table generated from 625 combinations of absorption ($\mu_a = 0.035 - 0.060\,\mathrm{mm}^{-1}$ with steps of $0.001\,\mathrm{mm}^{-1}$) and reduced scattering ($\mu_s' = 2.2 - 3.4\,\mathrm{mm}^{-1}$ with steps of $0.05\,\mathrm{mm}^{-1}$) coefficients. Figure 7a shows the average of experimentally detected ARR profiles for four dermis samples along with ± 1

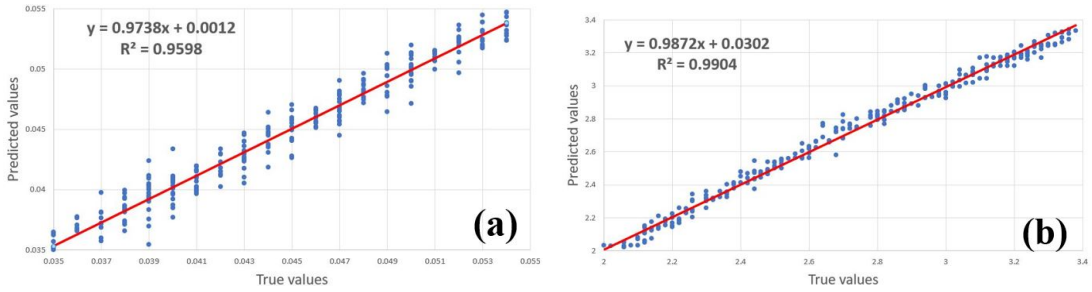

Figure 6. Predicted vs true values detected by random forest classifier for (a) absorption and reduced scattering coefficient.

standard deviation from 5 repeated measurements. All experimental and simulated ARR profiles are normalized with respect to experimental and simulated ARR profile for phantom 2, and transmitted profiles are normalized with respect to phantom 3.

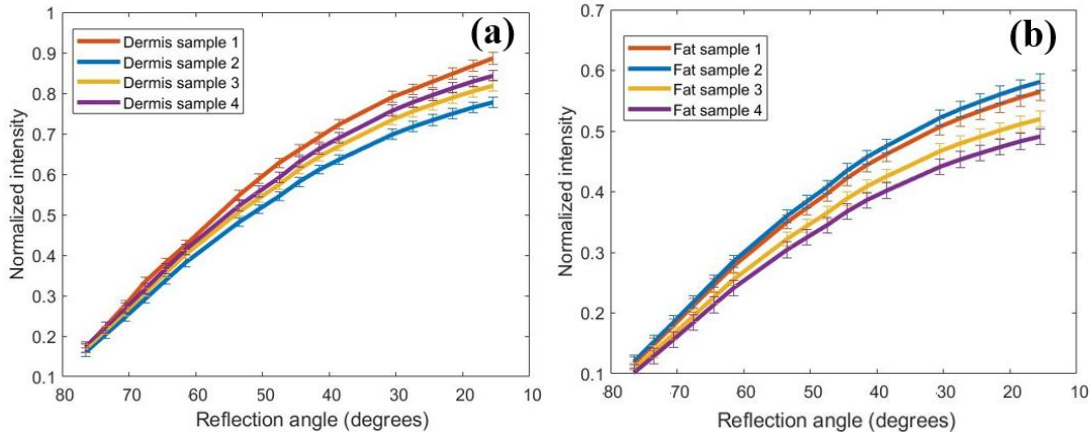

Figure 7. Measured ARR profiles for 4 samples of (a) dermis and (b) fat.

2.3.2 Subcutaneous fat

Both MC-ART (RMSE scan) and IS-IAD method were applied to subcutaneous porcine fat to obtain the corresponding μ_a and μ_s'. ART scan was implemented over a look-up table containing 500 combinations of $\mu_a = 0.035 - 0.06\,\mathrm{mm}^{-1}$ with steps of $0.001\,\mathrm{mm}^{-1}$, and $\mu_s' = 0.60 - 1.6\,\mathrm{mm}^{-1}$ with steps of $0.05\,\mathrm{mm}^{-1}$. Figure 7b shows the experimentally detected ARR profile for four fat samples along with ± 1 standard deviation. For the fat, while excited in the visible region, lower μ_a and μ_s' have been reported compared to dermis (DeLisi et al., 2019). Therefore, as one may expect to observe a highly forward scattering behavior for fat samples resulting in lower intensity ARR profiles (Figure 7b). As a validation of the extracted results, Table 2 shows the average and ± 1 standard deviation for extracted μ_s' and μ_a for all samples by both MC-ART and IS-IAD techniques.

	IS-IAD	
Tissue	μ_s' (mm^{-1})	μ_a (mm^{-1})
Dermis	**2.56** ± 0.099	**0.0505** ± 0.0023
Fat	**0.964** ± 0.109	**0.041** ± 0.003

	MC-ART (RMSE)		MC-ART (RF)	
Tissue	μ_s' (mm^{-1})	μ_a (mm^{-1})	μ_s' (mm^{-1})	μ_a (mm^{-1})
Dermis	**2.41** ± 0.135	**0.046** ± 0.0031	**2.38** ± 0.110	**0.047** ± 0.0032
Fat	**0.875** ± 118	**0.0385** ± 0.0030	**0.891** ± 0.126	**0.038** ± 0.0034

Table 2. Optical properties extracted for dermis and fat.

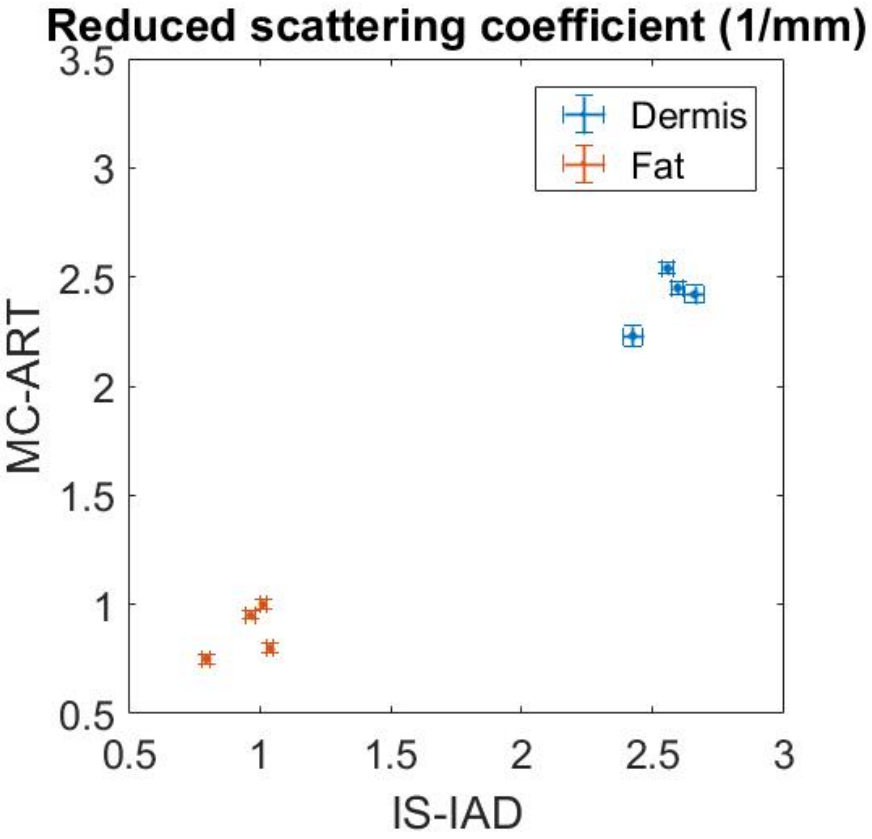

Figure 8. Absorption coefficient $\mu_a\,(\mathrm{mm}^{-1})$ detected for dermis (blue) and fat (red) by MC-ART and IS-IAD methods.

2.4 Discussion

The optical properties extracted by IS-IAD method were considered as the ground truth. Therefore, as a validation of the proposed system, MC-ART results using RMSE scan and machine learning method were compared with IS-IAD results by measuring intra-sample and inter-sample variations. The intra-sample variability of MC-ART (RMSE) vs IS-IAD is obtained by repeating each sample measurement five times and calculating their respective μ_a and μ_s' mean and standard deviation as shown in Figures 8 and 9. It should be noted that intra-sample variability was mainly attributed to the shot noise of each system. MC-ART intra-sample variability for μ_a is showed by vertical error bars (fat $\sim 6\%$, dermis $\sim 5\%$), which is in close match with IS-IAD with horizontal error bars, (fat $\sim 5\%$, dermis $\sim 3.5\%$) in all cases (Figure 9 bottom). The standard deviation detected for μ_s', for both methods, were measured to be nearly 2%, with $< 1\%$ difference (Figure 8 top). This shows that both methods, in terms of intra-sample variability, give a lower value for reduced scattering and relatively higher for absorption coefficient.

The inter-sample variability of dermis and fat is shown in Table 2 for MC-ART using both

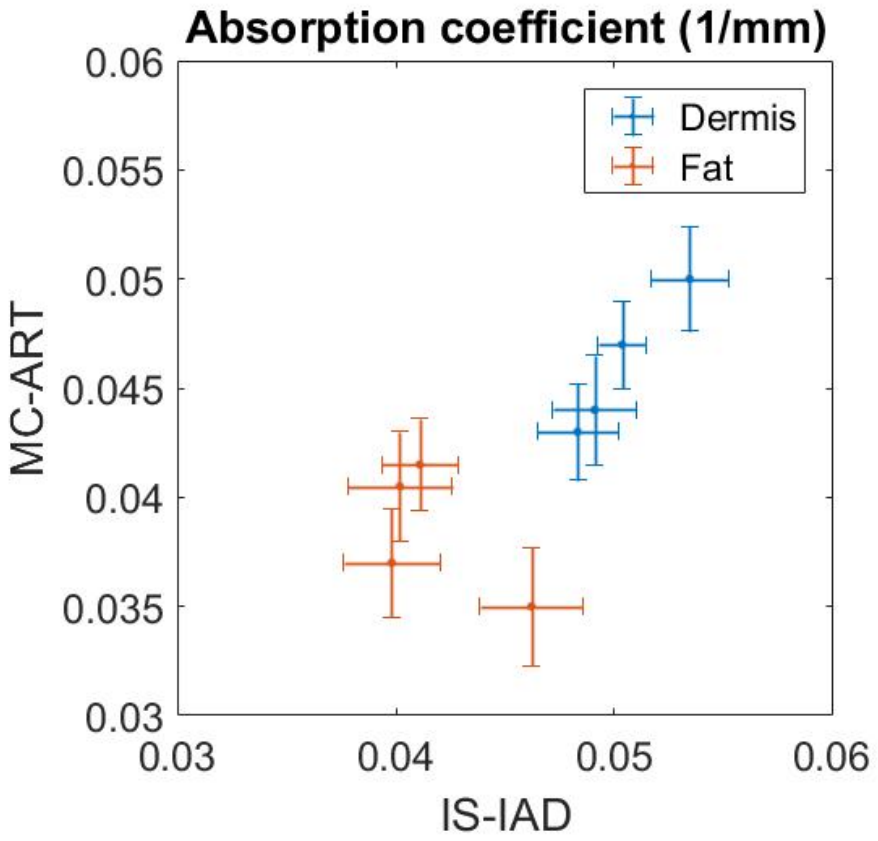

Figure 9. Reduced scattering coefficient $\mu_s'\,(\mathrm{mm}^{-1})$ detected for dermis (blue) and fat (red) by MC-ART and IS-IAD methods.

RMSE scan and RF classifier vs. IS-IAD method. This table shows average values of μ_a and μ_s' detected for 4 samples along with ± 1 standard deviation. It is observed that MC-ART with RMSE scan shows $< 7.5\%$ deviation, and RF classifier shows $< 7.1\%$ deviation from IS-IAD method when detecting μ_s' and μ_a. When comparing inter-samples results it is proven that MC-ART, by either RMSE scan or RF classifier, are in good match with IS-IAD results by having less than 10% deviation.

2.5 Future Work

In this research, a limited number of phantoms and tissue samples were studied. Future investigations are necessary to validate our conclusions with a more biologically relevant data set. This can be done by expanding the range of optical properties for both simulations and the created phantoms to μ_a: 0.01 – 0.08, μ_s': 0.5 – 8.0 mm^{-1}.

Future studies could also investigate the association between camera shot noise and the variability of the optical properties detected. This could be done by applying longer integration times or average over multiple acquisitions and look at the effect on the system

output. The effect of scanning steps of the MC look-up table could also associate with the variability of the optical properties detected.

In addition, a range of sample thickness might prove an important area for future research. The expansion of this system can be studied for optically thick samples where optical property detection is possible by detecting reflected signal only.

3.0 TIME DEPENDENT RADIATIVE TRANSFER MODELING

For the second effort of this project, we produced two models of time dependent propagation of light. The first is an analytic treatment of a one dimensional slab. This was useful for gaining basic insight into the problem, but is of limited usefulness for laboratory applications, as it deals with a uniformly illuminated infinite slab. The second model is a numerical treatment of a finite disk illuminated by a thin beam along the disk's axis. This provides a reasonable approximation of a laboratory sample. We describe both of these below, but first, we introduce the Radiative Transfer Equation, which governs the propagation of light for both calculations.

3.1 The Radiative Transfer Equation

The propagation of light is governed by the Radiative Transfer Equation, which is a statement of energy conservation: the change in intensity of a ray of light is the difference of the light emitted and the light absorbed at any given position. In integral form and with time dependence included, this is

$$I(\boldsymbol{x},t) = \int_0^{\tau_m} d\tau\, e^{-\tau} S(\boldsymbol{x}',t-\Delta t), \tag{1}$$

where I is the intensity (power per area per solid angle) of the radiation field at a given position and time, $\boldsymbol{x}$ is the spatial position (a vector in the general case), t is time, τ is optical depth (*i.e.* the integral of the opacity) measured along a ray from $\boldsymbol{x}$ to $\boldsymbol{x}'$, τ_m is the optical depth at the edge of the sample, S is the source function, describing the scattered or otherwise emitted light, and $\Delta t = s/c$, where s is the path length along the ray from $\boldsymbol{x}$ to $\boldsymbol{x}'$, and c is the speed of light.

Note that throughout this report we will use $\int dx\, f(x)$ to indicate the integral over $f(x)$ with respect to x. This notation is common in theoretical physics and gives a better sense of the integral as an operator than $\int f(x)\, dx$. We will also omit the integration limits to indicate an integral over all possible values.

In a scattering medium, the source function is

$$S(\Omega,t) = S_0 + \alpha \int d\Omega' d\Delta t\, \sigma(\Omega,\Omega',\Delta t) I(\Omega', t+\Delta t), \tag{2}$$

where S_0 represents external illumination, Ω and Ω' are the outgoing and incoming solid angles (*i.e.* ray directions), α is the albedo (*i.e.* the fraction of the total opacity due to

scattering), and σ is the scattering phase function. The integral is over all solid angles. This differs from the steady state in that we take into account the amount of time that scattering may take, although we will assume this is negligible in our calculations below. Note that we have also assumed the scattering medium itself is not changing on light travel timescales.

For all its complexity, radiative transfer is linear, *i.e.* the radiation field, and therefore the amount of light emitted from a sample scales linearly with the source function. We will use this in two ways. For the one dimensional slab, it will allow us to decompose the external illumination of the slab into Fourier components. For the numerical treatment, it will allow us to iteratively compute S for singly, double, etc. scattered light and then sum the result.

3.2 One Dimensional Slab

For simplicity, let us begin with a uniform, horizontally infinite slab, illuminated from above by collimated light perpendicular to the surface. Furthermore, let us assume in

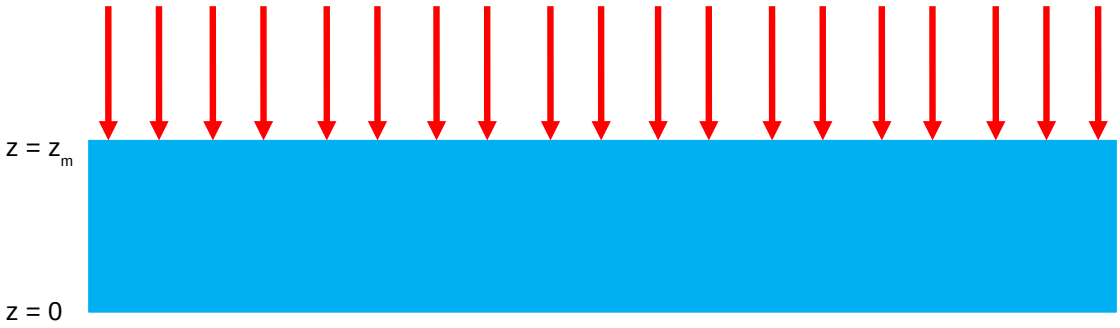

Figure 10. The simplest geometry to consider is a one-dimensional slab, uniformly illuminated from the top surface.

Let us examine a source function whose time dependence is sinusoidal:

$$S(\boldsymbol{x},t) = \hat{S}(\boldsymbol{x})e^{i\omega t} \tag{3}$$

where $\hat{S}(\boldsymbol{x})$ describes the spatial dependence, and ω is the angular frequency. As written, S is complex, but as usual in Fourier analysis, we can later add a corresponding source function that cancels the imaginary component. Using exponentials instead of sines and cosines greatly simplifies the math.

Substituting this into Equation (1) and assuming the opacity, κ, is at least piecewise constant so $\tau = \kappa s$ we get

$$\hat{I}(\boldsymbol{x}) = \int_0^{\tau_m} d\tau\, e^{-\gamma\tau}\hat{S}(\boldsymbol{x}') \tag{4}$$

where $I(\boldsymbol{x}) = \hat{I}(\boldsymbol{x})e^{i\omega t}$ and we have introduced $\gamma = 1 + i\omega/\kappa c$ for convenience. Note that γ is unitless, complex, and constant for a given ω. The characteristic length scale of the oscillating light is $\omega/\kappa c$. When this is much larger than an optical depth of 1, $\omega \ll \kappa c$, so the imaginary component of γ is negligible, and we approach the steady state case. When $\omega \gg \kappa c$, we can fit many oscillations within a single optical depth, the real component of γ is negligible, and oscillatory behavior dominates.

Because the Radiative Transfer Equation is linear, we need only examine one frequency component at a time. The source function due to external illumination of our slab is then:

$$\hat{S}_0(z,\mu) = \delta(z - z_m)\,\delta(\mu - 1), \tag{5}$$

where δ is the Dirac delta function, z is the spatial coordinate perpendicular to the slab, ranging from zero at the bottom to z_m at the illuminated surface, and $\mu = \cos\theta$, where θ is the polar angle. Note that we will use the convention that μ describes the "look" direction, which is opposite the direction light is propagating along a ray. Therefore, downward propagating rays have $\mu = 1$ because we look up to see them.

We can now use Equation (4) to compute the radiation field due to external illumination. The delta functions in Equation (5) mean that the only rays of interest will be traveling downward, so $\tau = \kappa(z_m - z)$ and the spatial integral is trivial:

$$\hat{I}_0 = e^{-\gamma\kappa(z_m - z)}\,\delta(\mu - 1) \tag{6}$$

The remaining delta function also makes Equation (2) trivial to evaluate, so the source function due to singly scattered light is

$$\hat{S}_1(z) = e^{-\gamma\kappa(z_m - z)} \tag{7}$$

We can apply Equation (4) once again to get the radiation field due to singly scattered light

$$\hat{I}(z,\mu) = \int_0^{\tau_m} d\tau e^{-\gamma[\kappa(z_m - z') + \tau]} \tag{8}$$

Using the fact that $z' = z + \mu\tau/\kappa$, we get

$$\hat{I}(z,\mu) = e^{-\gamma\kappa(z_m - z)} \int_0^{\tau_m} d\tau e^{-\gamma(1-\mu)\tau} \tag{9}$$

which we can integrate to obtain

$$\hat{I}(z,\mu) = \frac{e^{-\gamma\kappa(z_m - z)}}{\gamma(\mu - 1)} \left[e^{-\gamma(1-\mu)\tau_m} - 1 \right] \tag{10}$$

Recall τ_m is the optical depth at which our ray leaves the slab, so

$$\tau_m = \begin{cases} \kappa(z_m - z)/\mu, & \mu > 0 \\ \infty, & \mu = 0 \\ -\kappa z/\mu, & \mu < 0 \end{cases} \tag{11}$$

Therefore for $\mu > 0$ (looking up)

$$\hat{I}(z,\mu) = \frac{e^{-\gamma\kappa(z_m - z)/\mu} - e^{-\gamma\kappa(z_m - z)}}{\gamma(\mu - 1)} \tag{12}$$

and for $\mu < 0$ (looking down)

$$\hat{I}(z,\mu) = \frac{e^{-\gamma\kappa(z_m - z/\mu)} - e^{-\gamma\kappa(z_m - z)}}{\gamma(\mu - 1)} \tag{13}$$

We can evaluate this at the surface of the slab to find the externally observable singly scattered light. At the top $z = z_m$ and $\mu < 0$, so

$$\hat{I}(z_m,\mu) = \frac{e^{-\gamma\tau_z(1-1/\mu)} - 1}{\gamma(\mu - 1)}\ ,\ \mu < 0 \tag{14}$$

where $\tau_z = \kappa z_m$ is the vertical optical thickness of the entire slab. At the bottom $z = 0$ and $\mu > 0$, so

$$\hat{I}(0,\mu) = e^{-\gamma\tau_z}\frac{e^{-\gamma\tau_z(1/\mu - 1)} - 1}{\gamma(\mu - 1)}\ ,\ \mu > 0 \tag{15}$$

Note that Equation (15) is undefined when $\mu = 1$, *i.e.* a face-on view of the bottom of the slab, so we must calculate it in the limit $\mu \to 1$. The simplest and most physically insightful way to compute this is by returning to Equation (9). If we set $\mu = 1$ and $z = 0$ there, we get:

$$\hat{I}(0,1) = e^{-\gamma\tau_z}\int_0^{\tau_m} d\tau \tag{16}$$

The integrand is constant because the source function is falling exponentially away from the illuminated top surface, but our view of it is also falling exponentially in the opposite direction, due to obscuration. The two effects cancel each other. So

$$\hat{I}(0,1) = \tau_z e^{-\gamma\tau_z} \tag{17}$$

The same result can be obtained by applying L'Hopital's rule to Equation (15).

For completeness, when $\mu = 0$, $\tau_m = \infty$. Equation (10) then becomes

$$\hat{I}(z,0) = \frac{e^{-\gamma\kappa(z_m - z)}}{\gamma} \tag{18}$$

so

$$\hat{I}(z_m,0) = \frac{1}{\gamma} \tag{19}$$

and

$$\hat{I}(0,0) = \frac{e^{-\gamma\tau_z}}{\gamma} \tag{20}$$

These results can also be obtained from Equations (14) and (15) in the limit $\mu \to 0$.

Finally, we can look at Equations (14) and (15) in the limits of a very optically thick or thin slab. For $\tau_z \to \infty$ Equation (14) becomes

$$\hat{I}(z_m, \mu) = \frac{1}{\gamma(1-\mu)} \ , \ \mu < 0 \tag{21}$$

If we introduce the unitless frequency $\hat{\omega} = \omega/\kappa c$, such that $\gamma = 1 + i\hat{\omega}$, then the frequency response of singly scattered light from the top of an optically thick slab is

$$|\hat{I}(z_m, \mu)|^2 = \frac{1}{(1-\mu)^2} \frac{1}{1+\hat{\omega}^2} \tag{22}$$

Thus an optically thick slab is a low pass filter with a half power cutoff at $\hat{\omega} = 1$ (see Figure 11). We can see one optical depth into the sample. The light travel time delay means that the backscattered light we see averages over the number of oscillations that fit into that one optical depth. Averaging over complete oscillations results in essentially no signal, but we do receive signal from oscillations that are larger than one optical depth.

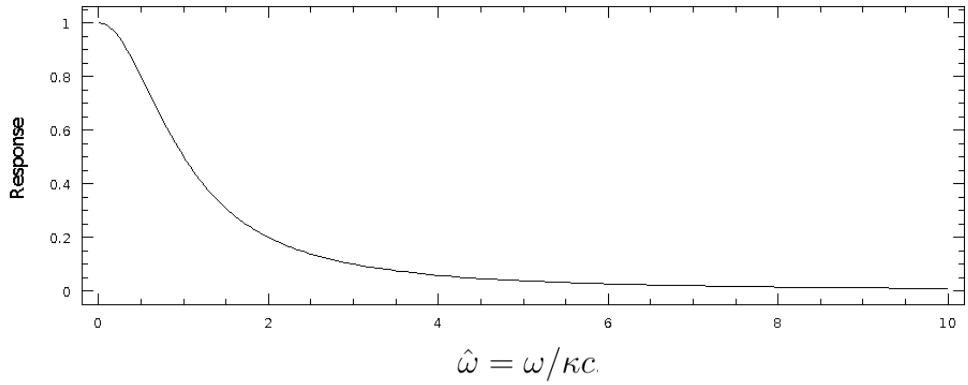

Figure 11. The frequency response of singly scattered light from the top of an optically thick slab, as computed in Equation (22)

In the optically thin limit $\tau_z \to 0$ we can approximate the exponential in Equation (14) by a first order Taylor series to get

$$\hat{I}(z_m, \mu) = \frac{-\gamma\tau_z(1-1/\mu)}{\gamma(\mu-1)} \tag{23}$$

which simplifies to

$$\hat{I}(z_m, \mu) = \frac{-\tau_z}{\mu} \tag{24}$$

Which passes all frequencies equally. Remember rays emanating from the top of the slab have $\mu < 0$ so $\hat{I}$ is positive. The flat frequency response is because the oscillations leave the bottom of the slab before they go through a complete cycle.

Similar analysis for the bottom of the slab shows that for $\tau \to \infty$ Equation (15) becomes

$$\hat{I}(0,\mu) = \frac{e^{-\gamma\tau_z}}{\gamma(\mu-1)} \tag{25}$$

giving a frequency response of

$$|\hat{I}(0,\mu)|^2 = \frac{e^{-\tau_z}}{(1-\mu)^2}\frac{1}{1+\hat{\omega}^2} \tag{26}$$

and in the optically thin limit:

$$\hat{I}(0,\mu) = \frac{\tau_z}{\mu}e^{-\tau_z} \tag{27}$$

These results are the same as for the top of the slab, except that the output is attenuated by $e^{-\tau}$.

3.3 Axisymmetric Geometry

Next, we will treat an axisymmetric geometry.

3.3.1 Defining the Problem

Consider a cylindrical sample illuminated by a laser beam entering the top face along the axis of the disk (see Figure 12). Let r and z be the usual cylindrical coordinates, with z ranging from 0 at the unilluminated face to z_m at the illuminated face and r ranging from 0 to r_m. Although symmetry lets us neglect the spatial azimuthal coordinate, Φ, we still need two coordinates, μ (again, the cosine of the polar angle) and ϕ (the azimuthal angle) to describe the angular distribution of the radiation field. Note that to maintain symmetry in Φ, ϕ is measured with respect to the vector from the cylinder axis and $\phi + \Phi$ is the direction with respect to the Cartesian x axis. We will assume the illuminating pulse has a Gaussian profile in r, t, and μ as follows:

$$I_{\text{ex}} = e^{-(r/\sigma_r)^2}\, e^{-(t/\sigma_t)^2}\, e^{-(\mu/\sigma_\mu)^2} \tag{28}$$

where σ_r, σ_t, and σ_μ are constant parameters specifing the widths of the Gaussians. Our goal is to compute the time dependent radiation field $I(r,z,\phi,\mu\ ,t)$. Note how we have gone from a two dimensional solution, $\hat{I}(z,\mu)$, for a slab to a five dimensional solution.

We will assume the scattering is instantaneous and depends only on $\Delta\mu$, the cosine of the angle between the incoming and outgoing rays, so we can write it as $\sigma(\Delta\mu)$. This is typical of biological samples, which lack a crystalline structure that could give a preferential

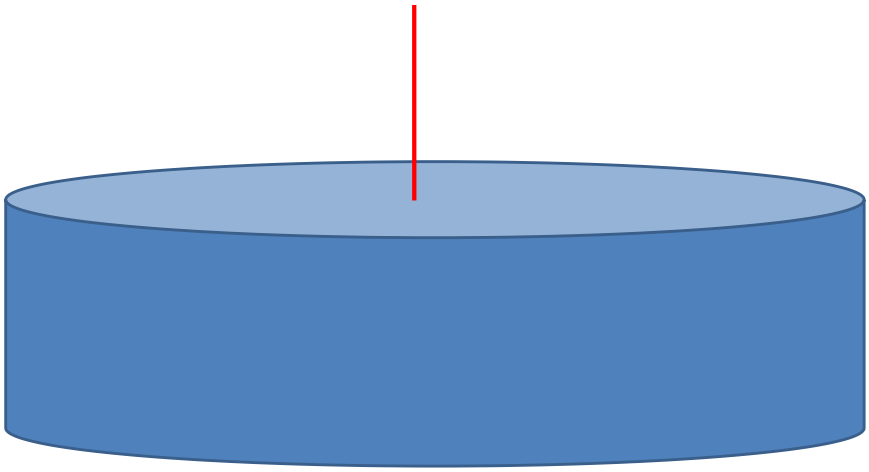

Figure 12. The geometry of our axisymmetric model.

direction in the material. Note that $\Delta\mu$ is *not* the difference in μ. We can derive $\Delta\mu$ by taking the dot product of two unit vectors. For a pair of rays with (μ_1, ϕ_1) and (μ_2, ϕ_2)

$$\Delta\mu = \mu_1\mu_2 + \cos(\phi_1 - \phi_2)\sqrt{(1-\mu_1^2)(1-\mu_2^2)} \tag{29}$$

As is customary in biophotonics, we will parameterize σ with the Henyey Greenstein function (Henyey and Greenstein, 1941) that was originally developed to describe scattering by interstellar dust. It uses a single parameter g to indicate the degree of forward or backward scattering such that

$$\sigma_{\mathrm{HG}} = \frac{1}{4\pi}\frac{1-g^2}{(1+g^2-2g\Delta\mu)^{3/2}} \tag{30}$$

Biological samples generally have strong forward scattering with g of 0.8 or higher.

While we did our analysis of singly scattered light from a slab analytically, we will have to resort to numerical integration to treat the disk. If we work in the Fourier domain, as we did for the slab, we would have to contend with subtractive cancellation and integrands that can be nonzero at large distance from the origin. We will therefore switch to the time domain.

3.3.2 Discretization

For numerical work to be tractable, we must discretize the problem at hand. Suppose we have a function $F(\boldsymbol{x})$ where $\boldsymbol{x}$ is a point in a multidimensional parameter space. Then we can approximate F as

$$F(\boldsymbol{x}) \approx \sum_i a_i f_i(\boldsymbol{x}) \tag{31}$$

Where the f_i are a set of pre-chosen basis functions, and the a_i are coefficients. This allows us to describe a function at an infinite number of points with a finite set of values,

the a_i.

For a set of basis functions to be useful, we must have a way of determining the a_i for an arbitrary F. In practice there are two ways of doing this. First, we could choose f_i that are orthogonal, such that

$$\int d\boldsymbol{x}\, f_i(\boldsymbol{x}) f_j(\boldsymbol{x}) = \begin{cases} 0, & i \neq j \\ 1, & i = j \end{cases} \tag{32}$$

where the integral is over all space. Then

$$a_i = \int d\boldsymbol{x}\, F(\boldsymbol{x})\, f_i(\boldsymbol{x}) \tag{33}$$

Familiar examples of orthogonal functions are spherical harmonics and Fourier series. Our other option is to choose basis functions such that

$$f_j(\boldsymbol{x}_i) = \begin{cases} 0, & i \neq j \\ 1, & i = j \end{cases} \tag{34}$$

for a pre-chosen set of points $\boldsymbol{x}_i$. In this case

$$a_i = F(\boldsymbol{x}_i) \tag{35}$$

We have just described an interpolation scheme, where by knowing the value of a function at a discrete set of points, we can approximate that function over all space.

In either case our goal is to choose a set of basis functions that can describe the problem at hand with a tractable number of a_i. When solving an integral equation, as we are here, we would also like the basis functions to be amenable to numerical integration.

Numerical integration works best over smooth functions, but smooth functions that satisfy either the orthogonality or interpolation criteria tend to oscillate, which can lead to subtractive cancellation errors. Our alternative is piecewise smooth interpolation basis functions. Here we define a grid in $\boldsymbol{x}$ space and allow the f_i to have discontinuous derivatives at the grid cell boundaries but require them to be smooth everywhere else.

The drawback of piecewise smooth basis functions in multidimensional radiative transfer is that we have the added burden of finding the grid cell boundaries along each ray over which we integrate. On the other hand radiative transfer solutions tend to have discontinuities at surface boundaries. For example, consider a horizontal ray on the top surface of a slab. The radiation field when looking slightly upward is zero, while it can be significantly non-zero when looking slightly into the slab. When dealing with such discontinuities, smoothness in basis functions is the enemy, as it can cause oscillations near the discontinuity.

This drove us to choose linear interpolation for our numerical solution of the axisymmetric geometry. In one dimension, the basis functions for linear interpolation are triangular, such that:

$$f_i(x) = \begin{cases} 0, & x < x_{i-1} \\ \frac{x-x_{i-1}}{x_i-x_{i-1}}, & x_{i-1} < x < x_i \\ \frac{x-x_{i+1}}{x_i-x_{i+1}}, & x_i < x < x_{i+1} \\ 0, & x > x_{i+1} \end{cases} \tag{36}$$

as illustrated in Figure 13.

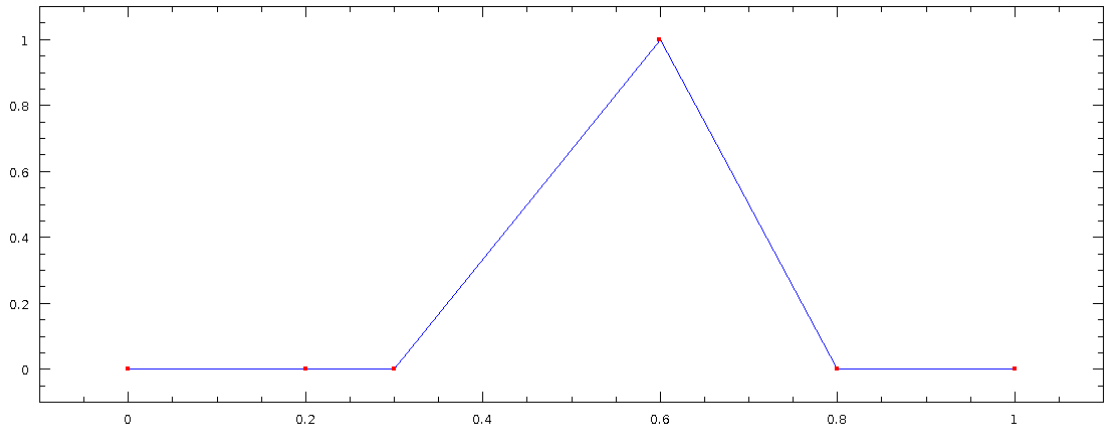

Figure 13. An example of a one dimensional linear interpolation basis function. Here we have chosen interpolation points at 0.0, 0.2, 0.3, 0.6, 0.8, and 1.0. We show the basis function that is non-zero at 0.6. The weighted sum of a set of these represents a linearly interpolated function.

We can extend this to multiple dimensions by choosing a rectangular grid and multiplying the basis functions for each dimension.

We discretize the radiative transfer equation (1) by interpolating the source function, such that

$$S(r,z,\phi,\mu,t) = \sum_j S_j f_j(r,z,\phi,\mu,t) \tag{37}$$

and the radiation field, such that

$$I(r,z,\phi,\mu,t) = \sum_i I_i f_i(r,z,\phi,\mu,t) \tag{38}$$

Then Equation (1) becomes the linear matrix equation

$$I_i = \sum_{ij} \Lambda_{ij} S_j \tag{39}$$

where

$$\Lambda_{ij} = \int_0^{\tau_m} d\tau\, e^{-\tau} f_j(\boldsymbol{x}', t - \Delta t), \tag{40}$$

where the ray origin and direction are specified by $(r, z, \phi, \mu, t)_i$. Note that because the f_i are known *a priori* we can compute the integral on the right hand side of Equation (40) numerically.

We follow a similar prescription to discretize the scattering equation (2) to get

$$S_i = \alpha \sum_{ij} \sigma_{ij} I_j \tag{41}$$

where

$$\sigma_{ij} = \int d\Omega' \, \sigma(\Omega_i, \Omega') \, f_j \tag{42}$$

In principle we could combine Equations (39) and (41) into a single linear equation that we could solve by inverting a matrix. This is a version of the Bohm-Vitense method (Mihalas, 1978). While this method has been successfully applied for steady state radiative transfer in axisymmetric geometry with an isotropic scattering function Pier and Krolik, 1992, it is intractable for the problem at hand. The number of dimensions in our solution space, $d = 5$. If each dimension needs n interpolation points to accurately represent the solution, then Λ_{ij} is an $N \times N$ matrix with $N = n^d$. Even if we could get away with $n = 10$, brute force inversion of a $10^5 \times 10^5$ matrix is challenging at best, as this is an $O(N^3)$ operation. When n reaches $10^{1.5}$, it takes significant resources to even store all 10^{15} elements of the matrix. Note that Pier and Krolik treated a steady state case with an isotropic thermal source function. The resulting $d = 2$ made for a much smaller lambda matrix.

What saves us is the fact that Λ_{ij} is extremely sparse. This is because each row represents a ray and the columns represent the points in parameter space that influence that ray. But a ray only passes through a small region of space, time, and direction. The sparsity is aided by our choice of linear interpolation basis functions. Higher order piecewise polynomials spread their influence over a larger number of points, and orthogonal basis functions and globally smooth interpolation (e.g. splines) spread the influence of each point globally. As a result, the number of non-zero elements of Λ_{ij} scales more like N than N^2.

We are able to solve Equations (39) and (41) using a variation of the lambda iteration technique (see Figure 14). We begin with the source function due to external illumination. We then use Equation (39) to compute the resulting radiation field, and then apply Equation (41) to find the source function for singly scattered light. We repeat this process to find the radiation field for singly scattered light and the source function for doubly scattered light. With each iteration, some energy leaves the disk, so with enough iterations we will find a scattering that does not contribute significantly to the total radiation field. The observable radiation field is the sum of all non-negligible scatterings. The main drawback of lambda iteration is that the number of iterations required scales with optical thickness. As we discuss in Section 3.3.6, we found that the practical limit that we could handle this way was a vertical optical thickness of 10.

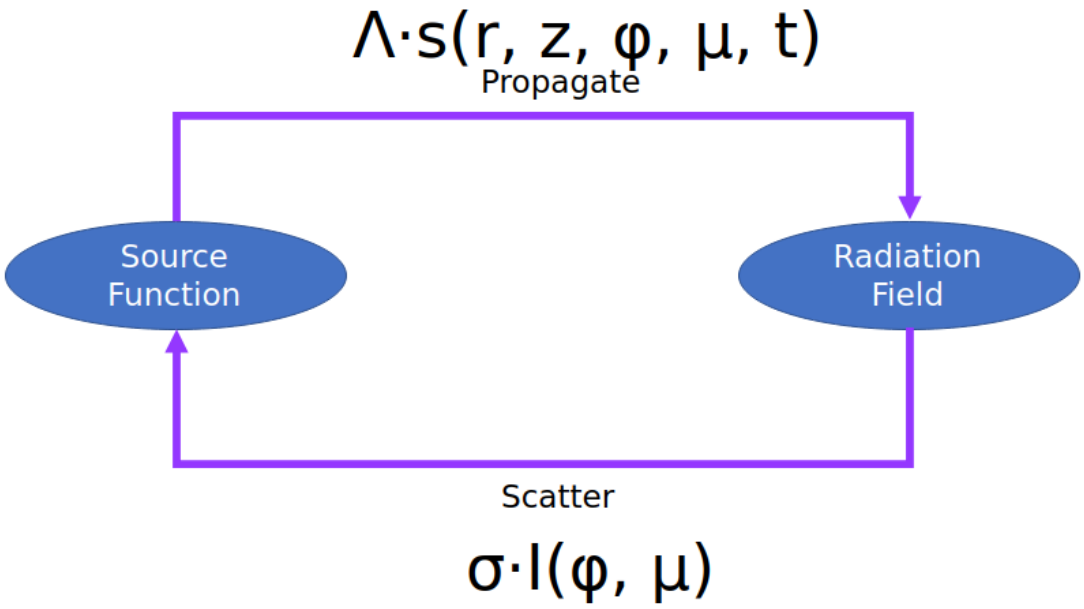

Figure 14. We used a variation on the lambda iteration technique, where we apply the lambda matrix to propagate successive scatterings of light and then apply the scattering matrix to determine the corresponding source function. The sum of the radiation field from each scattering is the observable radiation field.

3.3.3 Ray Geometry

Before we begin iterating, we must compute the lambda matrix. The ray integral in Equation (40) requires us to know how the various coordinates propagate along a ray. In other words if (r,z,t,μ,ϕ) describe the position of an observer and their look direction, then we need to compute the corresponding (r',z',t',μ',ϕ') at a distance s along that direction. This in turn allows us to compute the basis functions for any given s. Note that without loss of generality, we can assume $\Phi = 0$, but in general $\Phi' \neq 0$.

The Cartesian coordinates along a ray are

$$\begin{aligned} x' &= s\cos\phi\sqrt{1-\mu^2}+r \\ y' &= s\sin\phi\sqrt{1-\mu^2} \\ z' &= \mu s+z \end{aligned} \tag{43}$$

Now $r'^2 = x'^2 + y'^2$, so

$$r'^2 = (1-\mu^2)s^2 + 2sr\cos\phi\sqrt{1-\mu^2}+r^2 \tag{44}$$

For time we have the usual light travel delay:

$$t' = t - \frac{s}{c} \tag{45}$$

For directions, μ is invariant:

$$\mu' = \mu \tag{46}$$

but

$$\phi' = \phi - \Phi' \tag{47}$$

where $\Phi' = \tan^{-1}(y'/x')$.

We also need to determine the value of s for which a ray crosses a grid cell boundary, so that we can integrate over each piecewise segment of our basis functions separately. We therefore need to invert the above equations to give s for each of the primed coordinates.

From Equation (44) we get

$$s(r') = \frac{-r\cos\phi \pm \sqrt{r'^2 - r^2\sin^2\phi}}{\sqrt{1-\mu^2}} \tag{48}$$

and from Equations (47) and (43) we get

$$s(\phi') = \frac{r\sin(\phi - \phi')}{\sin\phi'\sqrt{1-\mu^2}} \tag{49}$$

although the same result is obtained more simply from the law of sines. Trivially,

$$s(z') = \frac{z' - z}{\mu} \tag{50}$$

and

$$s(t') = c(t - t') \tag{51}$$

We do not need $s(\mu')$ because a ray always straddles a single μ grid boundary.

3.3.4 Conservation of Energy

To validate our models, we compare the total light energy in the illuminating laser pulse to the flux emitted from the sample integrated over all surfaces and over all time. Conservation of energy dictates that the two should be the same. Discrepancies can reveal errors in our analytic calculations, bugs in our code, or inaccuracies due to an insufficient number of grid points.

The flux through a surface is given by

$$F(\hat{\boldsymbol{n}}) = \int d\Omega\, I(\Omega)\hat{\boldsymbol{x}}(\Omega)\cdot\hat{\boldsymbol{n}} \tag{52}$$

where $\hat{\boldsymbol{x}}(\Omega)$ is the unit vector pointing in the direction of light propagation along a ray, and $\hat{\boldsymbol{n}}$ is the outward-facing normal to the surface. The integral is over all solid angles.

For the top surface $\hat{\boldsymbol{x}} \cdot \hat{\boldsymbol{n}} = -\mu$. The negative sign arises because we have adopted the convention that μ points in the look direction, while $\hat{\boldsymbol{x}}$ points in the propagation direction. For the bottom surface $\hat{\boldsymbol{x}} \cdot \hat{\boldsymbol{n}} = \mu$ because in this case $\hat{\boldsymbol{n}}$ points downward.

For the outer rim of the sample, $\hat{\boldsymbol{x}} \cdot \hat{\boldsymbol{n}} = -\sqrt{1-\mu^2}\cos\phi$ Again, the negative sign is because ϕ designates the look direction.

After we compute the radiation field for each scattering we can numerically integrate the flux over each surface (top, bottom, side) and over all time in order to get the total energy emitted for that scattering. We use this as our stopping criterion, iterating until the energy emitted by a scattering is 0.1% of the illuminating energy. We sum the scatterings to get the total emission. We consider a model to be successful if the total emitted energy is within a few percent of the illuminating energy.

3.3.5 Software Optimizations

The biggest challenge in coding the calculations described above is optimizing memory usage. While we can compensate for runtime inefficiencies by simply running the simulations longer (within the limitations of the project duration), memory is a finite resource.

Our first optimization is to take advantage of the sparseness of the lambda matrix. We only store non-zero matrix elements. However, this requires us to also store the coordinates of each element. A naive implementation of this would require 10 floating point numbers or 40 bytes for each non-zero element, even at single precision.

We used the following insights to optimize the lambda matrix indexing:

1. Each coordinate corresponds to a pre-chosen grid point that can be specified by an integer index for each dimension.
2. We only need to specify the origin and direction of a ray once per row
3. The lambda matrix depends only on relative differences in time, $t' - t$, not t or t' individually, as long as the time grid is evenly spaced.

We store the lambda matrix on disk with the following format (see Figure 15). First, we write the grid indexes of μ, r, z and ϕ, each encoded as an 8 bit unsigned integer. Note that we do not need to record t as only relative times matter. After this we write the data in the row, alternating element coordinates and element values. The element coordinates give the grid index of r', z', $t' - t$, and ϕ'. Note that we do not need to record μ' because

$\mu' = \mu$. We encode these in an unsigned 32 bit integer, using just enough bits to encode the maximum grid index for each coordinate. We store the lambda matrix elements as 32 bit single precision floating point numbers.

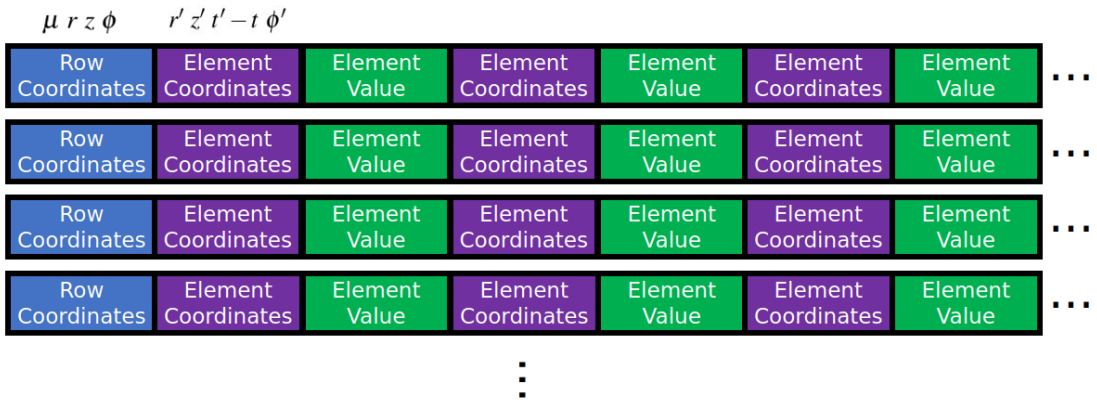

Figure 15. The data format for the lambda matrix. We store row and column coordinates separately packing their grid indices into 32 bit unsigned ints. Element values are stored as 32 bit floating point numbers

While generating the lambda matrix we write each row when we are done computing it and then flush it from memory. Similarly, while applying the lambda matrix, we read rows as needed and then flush them from memory when we are done with t hem. This means we need to read the lambda matrix from disk for each scattering iteration. Although this adds I/O overhead, it is necessary, as the entire matrix is too large to fix in memory at the same time.

Oceanit's cluster nodes have dual hex core Xeon processors, giving 12 real cores and 24 hyperthreads. We designed our code to take advantage of these cores on a single node. We designed a custom scatter-gather parallelization infrastructure, which launches arbitrary processing jobs (defined by software objects) in separate threads, waits for the jobs to complete, and collects their results. The jobs we implemented partitioned work at the lambda matrix row level, either generating or applying a single row at a time. We did not make the extra effort of allowing the code to spread work across multiple nodes, as it was more efficient to run more than one model at the same time, each on its own node.

3.3.6 Models

Without loss of generality, we scale energy so that the illuminating pulse contains an energy of 1. We scale distance such that the thickness of the disk is 1, and choose time units such that $c = 1$.

The parameters of a model are the aspect ratio r_m/z_m, the vertical optical thickness τ_z, the scattering parameter, g, and the widths of the r, μ and t Gaussians for the illuminating

pulse (σ_r, σ_μ, and σ_t, respectively). We used $r_m/z_m = 5$ for all of our models. While this is a largely arbitrary choice, it captures the flat nature of likely laboratory samples, and larger aspect ratios are not likely to reveal significantly different behavior, as most of the radiation left the disk through the top and bottom faces in our models.

We also chose $\sigma_r = 0.1$, $\sigma_\mu = 0.005$, and $\sigma_t = 0.1$. Thus the effective radius of the pulse was $1/50$ of the radius of the disk, and its duration was 1/10 of the light travel time through the disk. Note that the linearity of the radiative transfer equation means that we can simulate longer duration pulses by convolving our solutions with arbitrary kernels in time. We attempted to use an infinitesimally thin and short pulse in early versions of our model, but this introduced singularities in the solution that could not be handled well numerically.

Thus the free parameters for our models were τ_z and g. We made two series of runs. The first kept $\tau_z = 1$ and let g run through the full range of 0.0, 0.1, 0.2, 0.3, 0.4, 0.5, 0.6, 0.7, 0.8, 0.9, and 0.95. Our main purpose for this run was to flush out bugs in our code by starting with the less numerically demanding isotropic scattering case and working our way toward more biologically relevant values of g. Our second set of runs had $g = 0.8$, 0.9, and 0.95 and let τ_z range through 0.01, 0.1, 2, 5, and 10. Note that the $\tau_z = 1$ case for these values of g was handled by our first run.

We used the same coordinate grid for all of our runs. The r, z, t, and ϕ grids were evenly spaced, with 101, 61, 201, and 51 points respectively. The μ grid had a higher density of points for downward propagating rays, in order to handle high values of g. We began with 51 μ points between -1 and 1. Then we recursively subdivided this grid such that $\sigma_{\mathrm{HG}}(\mu)$ with $g = 0.9$ can be linearly interpolated on the refined grid with an accuracy of 1% (see Figure 16). The resulting grid has 168 points as shown in Figure 17.

Note that there are over 10 billion points in each solution. We output the radiation field at all of these points at the end of each iteration using single precision floating point numbers. With additional metadata, each solution file required about 110 Gigabytes of storage. A naively stored lambda matrix would require 4×10^{20} bytes. With the sparse storage scheme we described in section 3.3.5, our lambda matrix files generally required 180 – 190 gigabytes, a compression of 9 orders of magnitude!

3.3.7 Results

For each of our runs with $\tau_z = 1$, Table 3 shows the number of scattering iterations we needed to compute before the emitted energy was below 0.001 of the total emitted energy. Note that all of the models conserve energy to better than 1%. The number of scatterings decreases as g increases, as photons are more likely to continue on the shortest path out the bottom of the disk after scattering.

Table 4 lists the runs with forward scattering over a range of τ_z. Note that the $\tau_z = 1$ runs

Table 3. Model runs with $\tau_z = 1$.

τ_z	g	Scatterings	Energy Conservation
1.0	0.0	13	100.5%
1.0	0.1	13	100.5%
1.0	0.2	12	100.5%
1.0	0.3	12	100.5%
1.0	0.4	12	100.5%
1.0	0.5	12	100.5%
1.0	0.6	12	100.5%
1.0	0.7	11	100.4%
1.0	0.8	11	100.4%
1.0	0.9	9	100.1%
1.0	0.95	8	99.8%

Table 4. Model runs with forward scattering for various τ_z

τ_z	g	Scatterings	Energy Conservation
0.01	0.8	2	97%
0.01	0.9	2	97%
0.01	0.95	2	97%
0.1	0.8	3	98%
0.1	0.9	3	98%
0.1	0.95	3	98%
1.0	0.8	11	100%
1.0	0.9	9	100%
1.0	0.95	8	100%
2.0	0.8	18	102%
2.0	0.9	16	102%
2.0	0.95	14	102%
5.0	0.8	39	102%
5.0	0.9	36	103%
5.0	0.95	32	103%
10.0	0.8	$>$69	$>$102%
10.0	0.9	66	101%
10.0	0.95	60	102%

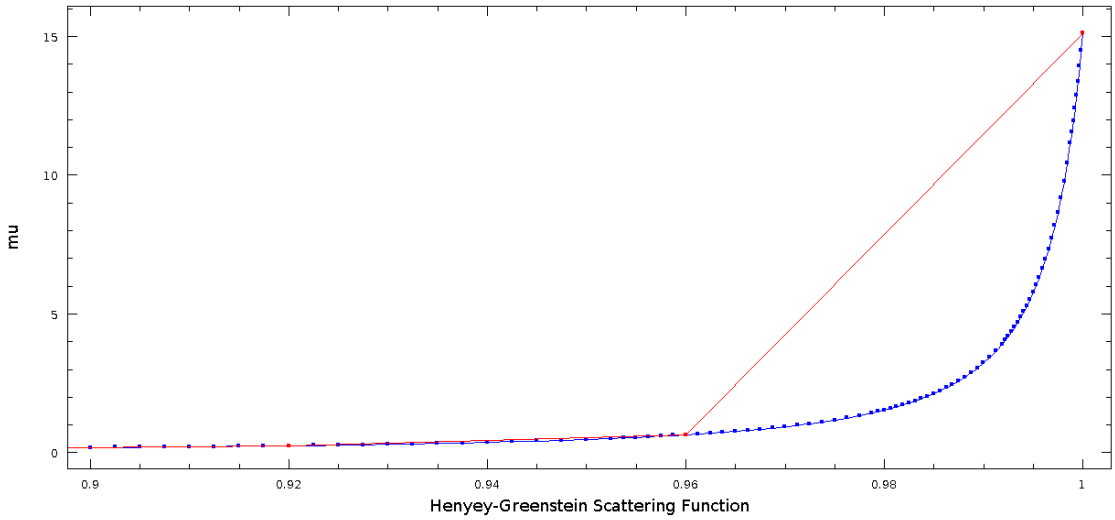

Figure 16. The Henyey-Greenstein scattering function with $g = 0.9$ shown on an unrefined 51 point μ grid (red) and on a grid recursively subdivided to interpolate the function accurately (blue). Note the large interpolation errors for $\mu > 0.96$ with the unrefined grid.

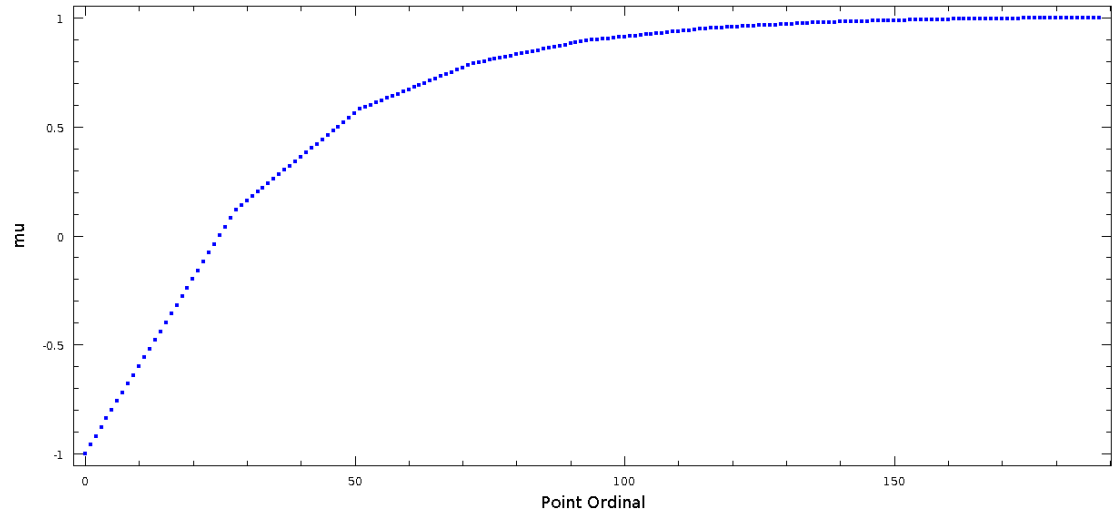

Figure 17. Our refined μ grid.

are copied from Table 3. The energy conservation was slightly worse here than for the $\tau_z = 1$ runs, likely because we tuned our coordinate grid on the former. Nevertheless, in all cases the models conserved energy to within a few percent, meeting our criterion for a successful run.

In one case, $\tau_z = 10$ $g = 0.8$, we terminated the calculation before reaching our stopping criterion that the emitted energy be below 0.001. Here the 69^{th} iteration emitted

0.00134092, with each successive iteration emitting 0.0001 less than the one before it. From this we infer that to strictly meet our stopping criterion we would have needed four more iterations, which would have added roughly half a percent to the energy conservation.

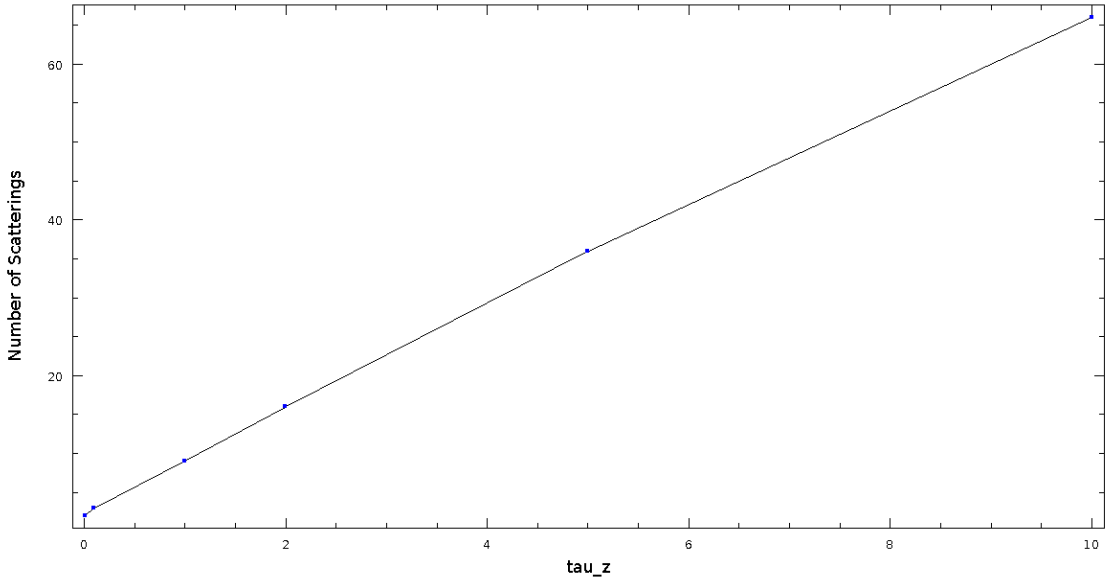

Figure 18. The number of scatterings to reach convergence as a function of τ_z with $g = 0.9$.

Figure 18 plots the number of scatterings to reach convergence as a function of τ_z for $g = 0.9$. Note how this is nearly linear, as we would expect for a strongly forward scattering medium. This is because scatterings do not usually change the direction of a photon significantly, so they proceed in a more or less straight line until they reach the bottom of the disk.

Contrast this with the random walk associated with isotropic scattering, where we would expect the number of scatterings to scale as τ_z^2. This has implications for running models with significant optical depth in non-biological samples. But note that in this case the radiation field within the sample would be close to isotropic. This would reduce the dimensionality of the problem, which might make a different approach tractable, such as the Bohm-Vitense method, whose computation is independent of optical thickness.

Figure 19 shows another aspect of the same phenomenon. The τ_z-th scattering emits the most energy. Again, photons usually continue in a straight line after scattering, so they scatter roughly τ_z times before the illuminating pulse punches through the bottom of the disk. Note that for high τ_z the light emitted in early scatterings can be less than 0.001. We had to specify a minimum number of scatterings to avoid triggering our stopping criterion when τ_z was 10.

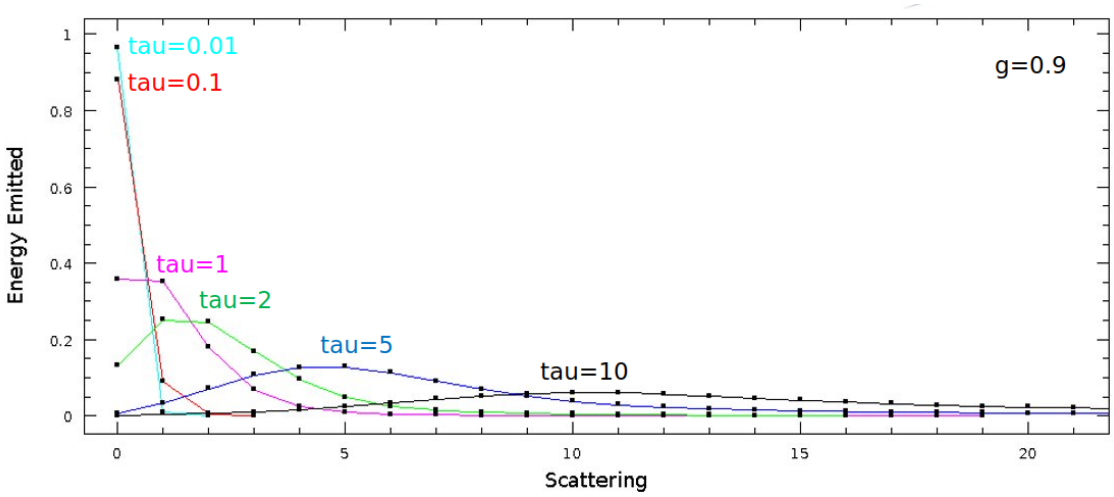

Figure 19. The energy emitted by each scattering for $g = 0.9$ and a range of τ_z.

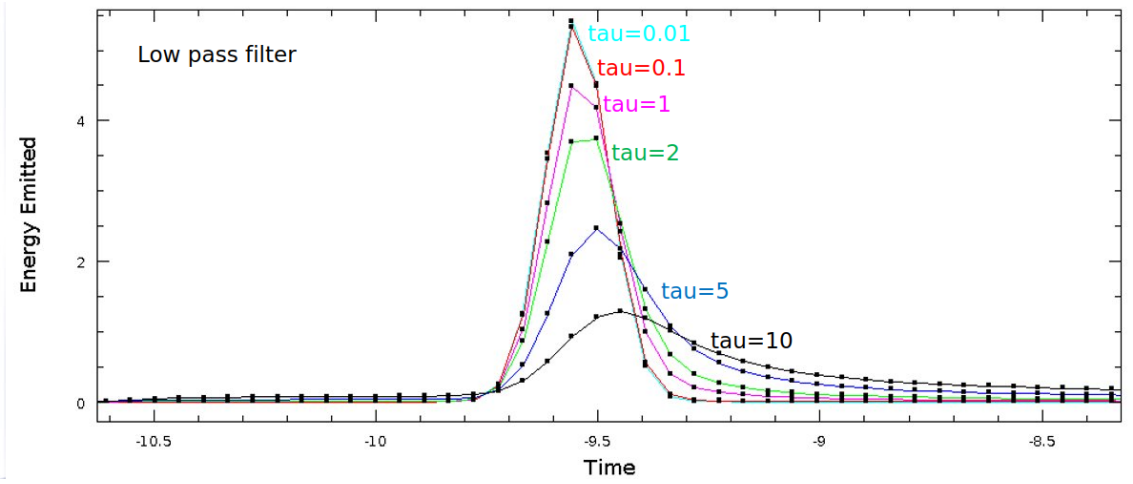

Figure 20. The energy emitted as a function of time for $g = 0.9$ and a range of τ_z.

Figure 20 shows the total power emitted from all scatterings as a function of time. The illuminating pulse strikes the top of the disk at around time -10.5 with a duration of roughly 0.1. For optically thin models we see this pulse largely unmodified as it leaves the bottom of the disk, delayed by the light travel time. As τ_z increases, the power peak broadens. Although we have strong forward scattering, there is still some deflection in the scattered photon's paths. This makes a broader distribution of the distance that photons travel before they leave the bottom of the disk, which in turn causes a broader distribution in time.

Figure 21 shows the power emitted as a function of time from the top, bottom, and side surfaces for the model with $\tau_z = 10$ $g = 0.9$. Notice how most of the energy leaves through the bottom in a pulse that is a somewhat broadened version of the illuminating

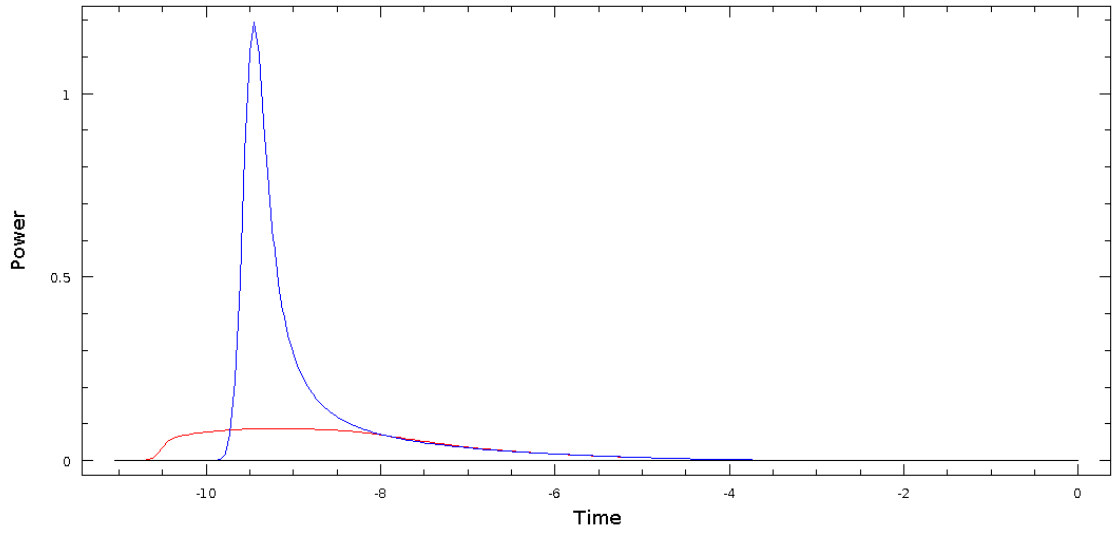

Figure 21. The power emitted from the top (red), bottom (blue), and side (black) of the disk for the $\tau_z = 10$ $g = 0.9$ model as a function of time

pulse, consistent with Figure 20. Here we are better able to see that the broadening is asymmetric with a sharp rise and a more gradual fall off. This is because scattering can only increase the distance a photon travels to reach the bottom surface.

The energy from the bottom surface shows a much broader profile. Energy begins leaving the top surface as soon as the illuminating pulse begins, unlike the bottom surface, where photons need to travel through the sample before they can exit. Here we are seeing the small amount of light that is scattered to the side or backwards. The broad peak comes from the range of distances that photons travel to return to the top surface. Note that the radiation from the top surface dies out as the main pulse leaves the bottom surface. This suggests that the light we see from the top surface has likely only has one errant scatter that redirected it toward the top, although it has likely experienced several downward scatters.

Finally, notice that the light from the edge of the disk is negligible. This supports our assertion that models with flatter aspect ratios (i.e. larger r_m/z_m) would not display significantly different phenomena. All of the light leaves through the top and bottom surfaces before it reaches the side.

Figure 22 shows the power emitted from the top surface as a function of time for the three values of g that we ran. Note that the power from the top surface decreases as g increases. This is as we would expect as greater forward scattering directs less energy back toward the surface.

More interestingly, the shape of the profile flattens as g increases. When $g = 0.8$ the

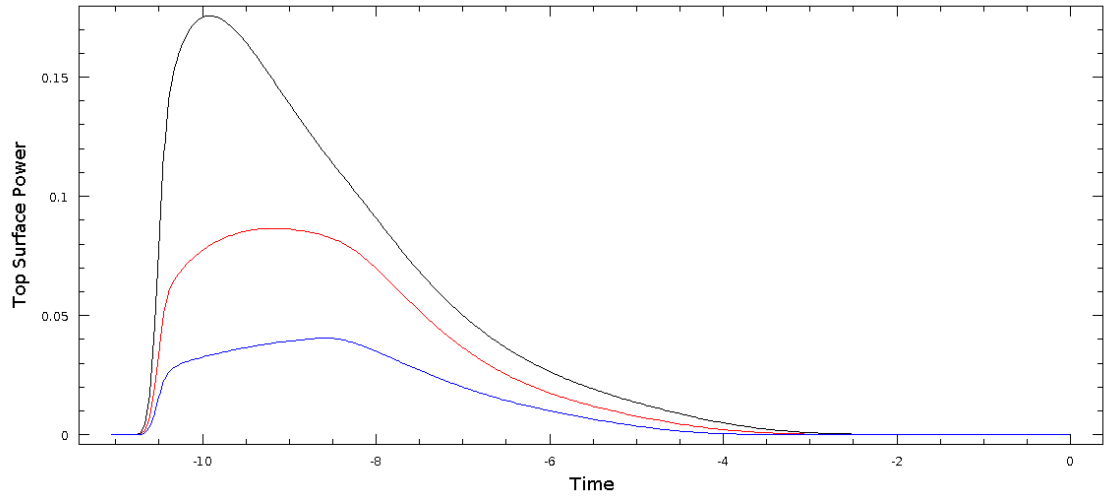

Figure 22. The power emitted from the top surface as a function of time for $\tau_z = 10$ and $g = 0.8$ (black), $g = 0.9$ (red), and $g = 0.9$ (blue).

profile has a high peak and a more gradual falloff, but when $g = 0.95$, there is a sharp rise followed by a gradual rise and then a gradual falloff. This is consistent with more energy being scattered back toward the top before it has penetrated too deep.

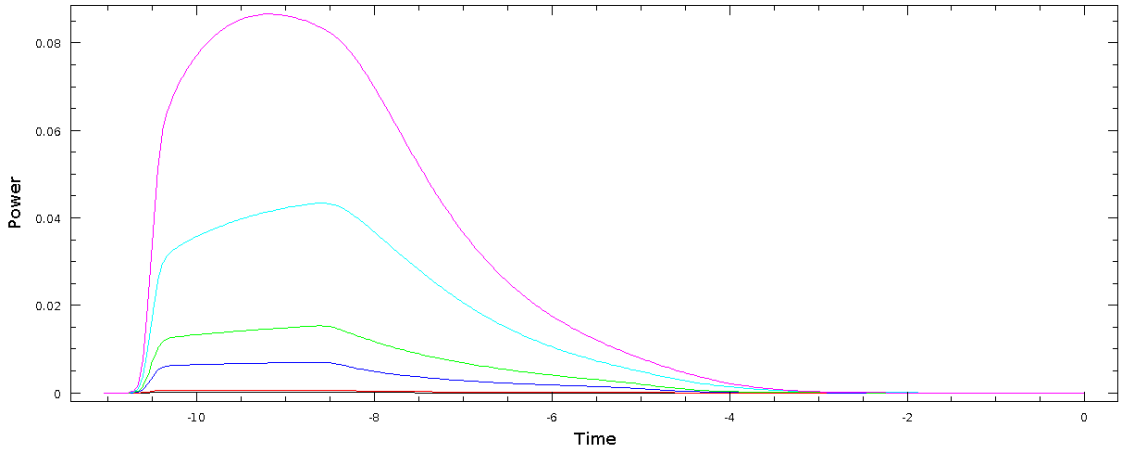

Figure 23. The power emitted from the top surface as a function of time for $g = 0.9$ and $\tau_z = 0.01$ (black), $\tau_z = 0.1$ (red), $\tau_z = 1.0$ (blue), $\tau_z = 2.0$ (green), $\tau_z = 5.0$ (cyan), and $\tau_z = 10.0$ (magenta).

We see similar behavior when we look at the time dependence of top emission as a function of optical thickness. The greater the optical thickness, the larger the number of scatterings, and the greater chance that a photon will be deflected back toward the top.

In biophotonics it is common to characterize this equivalence between increasing g and decreasing optical thickness with the reduced scattering coefficient. The idea is to model

forward scattering as a delta function in the forward direction plus an isotropic scattering component, with g being the fraction of scattered light going directly forward. As directly forward scattering has no effect on the path of a photon, we essentially have isotropic scattering with an opacity reduced by $1-g$.

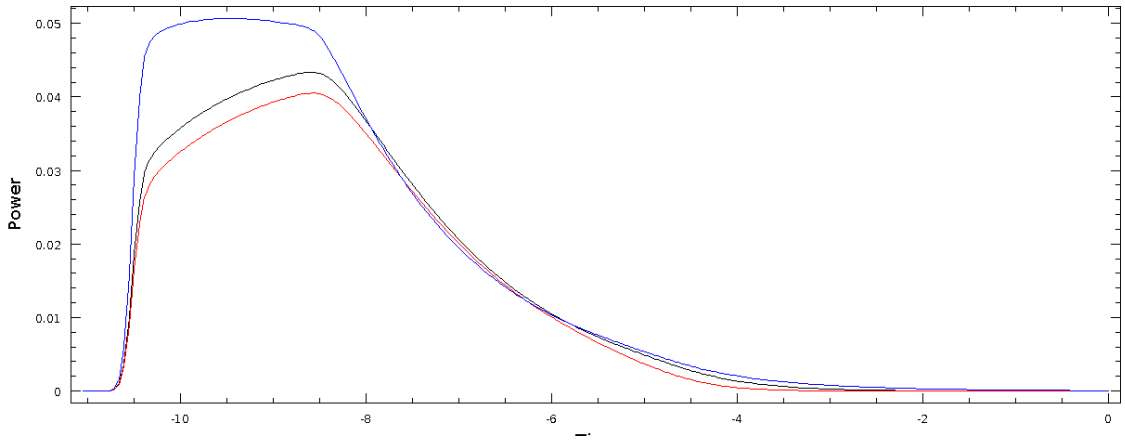

Figure 24. The power emitted from the top surface as a function of time for $g = 0.95$ $\tau_z = 10.0$ (black), $g = 0.9$ $\tau_z = 5.0$ (red), and $g = 0.5$ $\tau_z = 1.0$ (blue). Note that all three have $\tau_z' = 0.5$.

In our notation we can define the reduced vertical optical thickness $\tau_z' = (1-g)\tau_z$. Figure 24 shows three models with $\tau_z' = 0.5$. The two with high values of g are qualitatively the same, though not identical. The delta function approximation breaks down when $g = 0.5$ and we see significantly different behavior.

To better understand the variation in the time profile of the top emission with τ_z', we show a visualization of the top emission as a function of time for fixed g and a range of τ_z in Figure 25. For very optically thin models, the emission is dominated by a single scattering of the illuminating pulse, so we see a small dot that fades with time. As τ_z increases, we also see doubly scattered light, appearing as an expanding ring, because it has been scattered into our line of sight after traveling some distance from the axis of the disk. As τ_z increases further, we see more scatterings, and the hole in the ring fills in as we see light deflected back from the ring and traveling inward before being again deflected into our line of sight.

Referring back to Figure 23 for optically thick models we see a smooth rise and fall as the multiple scatterings are muddled together. For lower optical thicknesses we see a sharp rise when the singly scattered core arrives, and a flat section as the doubly scattered ring expands, and then a falloff as it looses light through the top and eventually the side.

Figure 25 also shows that we can use ultra high speed imaging to infer τ_z' for a sample. If the backscattered light appears as a uniform expanding circle, then $\tau_z' \gtrsim 1$. If only a small spot the size of the illuminating beam appears, then $\tau_z' \ll 1$. If an expanding ring is

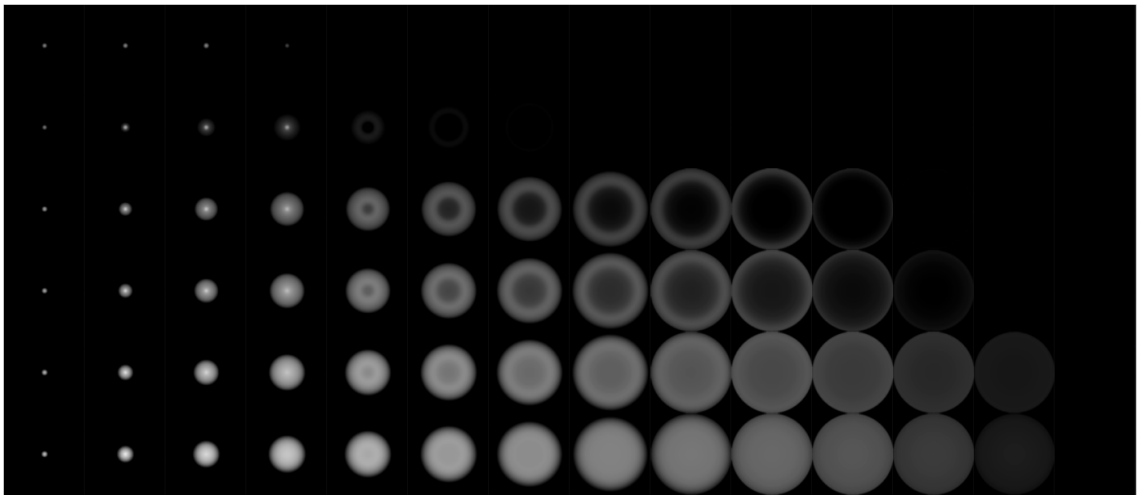

Figure 25. Frames from videos of the emission from the top of the sample for models with $g = 0.9$ and, from top to bottom, $\tau_z = 0.01$, $\tau_z = 0.1$, $\tau_z = 1.0$, $\tau_z = 2.0$, $\tau_z = 5.0$, and $\tau_z = 10.0$. Time increases to the right. This is how the sample would appear when viewed from directly overhead. We assumed an equal light travel delay from each point on the surface to the observer. This assumption is accurate when the observer's distance from the sample is much greater than r_m. We scaled the brightness logarithmically with white to black corresponding to 7.4 decades.

visible, then $\tau_z' \lesssim 1$

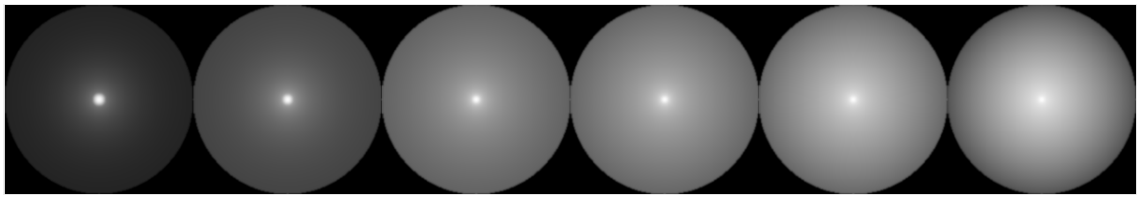

Figure 26. The time integrated top views of the same models as in Figure 25. From left to right: $\tau_z = 0.01$, $\tau_z = 0.1$, $\tau_z = 1.0$, $\tau_z = 2.0$, $\tau_z = 5.0$, and $\tau_z = 10.0$. All models have $g = 0.9$. We used the same 7.4 decade log scaling as in Figure 25, but here we scaled the brightest pixel in each model to be white.

Contrast the information we can get from ultra high frame rate video with the time integrated images in Figure 26. These images represent what we would observe with a conventional camera or if the sample were illuminated with a continuous beam. The images appear qualitatively similar with the major difference being the ratio between the brightness of the center peak and the diffuse scattered light. However this would be challenging to measure as we would have to determine a brightness ratio of several orders of magnitude. A camera would need high dynamic range to keep the diffuse emission above the noise floor without saturating the peak. Overall brightness with respect to the illuminating pulse could be used to infer τ_z', but this would require independent absolute measurement of the energy in the illuminating pulse as well as an absolute photometric calibration of the camera.

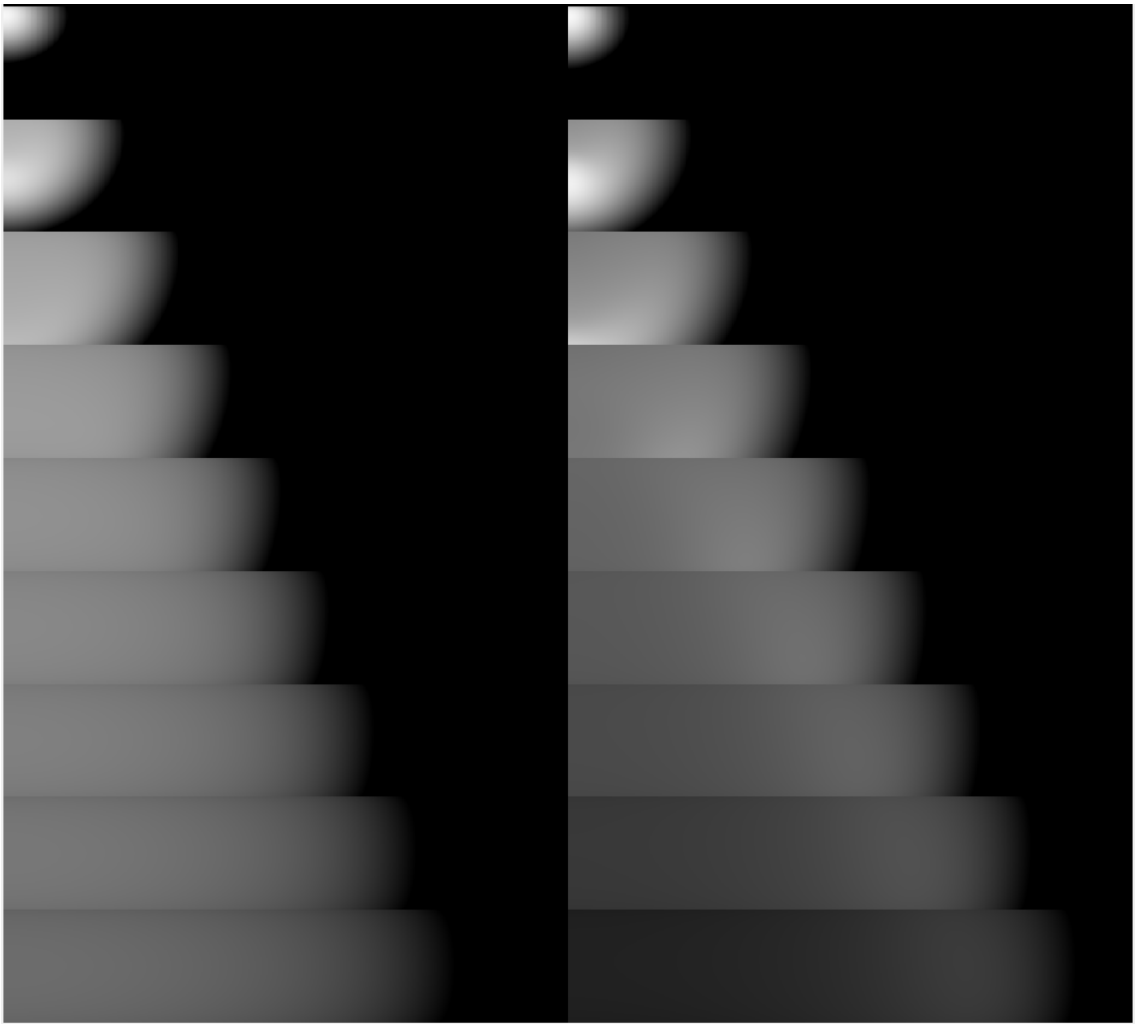

Figure 27. The photon density in the interior of the disk for the model with $\tau_z = 1$ $g = 0.8$ (left) and $\tau_z = 10$ $g = 0.95$ (right). Time increases downward with each step representing 0.55 time units. Each slice has $r = 0$ and $z = 0$ at the bottom left corner. Brightness is scaled logarithmically, with black to white ranging over 7.4 decades as in Figure 25

Finally, to see how light propagates within the disk, we can integrate over all solid angles to compute the angle averaged intensity:

$$J(r,z,t) = \int d\Omega I(r,z,t,\mu,\phi) \tag{53}$$

which is proportional to the energy density and the photon density for monochromatic light. Figure 27 shows J for the models with $\tau_z = 10.0$, $g = 0.8$, and therefore $\tau_z' = 2.0$ and with $\tau_z = 10.0$, $g = 0.95$, and therefore $\tau_z' = 0.5$. For both models we see an expanding front of scattered light. In the lower τ_z' model the initial pulse is visible as a bright spot in the early frames as it propagates downward, but it is far less prominent in the higher τ_z' model. Also in the lower τ_z' model the edge of the expanding front is brighter than

the interior, but for higher τ_z' the expanding region is more uniform, presumably because it has undergone more scatterings in the non-forward direction. This is consistent with Figure 25.

3.4 Conclusions

Our models have shown that picosecond imaging can reveal information about the optical properties of a sample that is not as readily apparent with traditional imaging. In particular even a single ultra-fast snapshot could be used to derive the reduced scattering coefficient of a sample based on the morphology of the propagating light. Even less expensive ultrafast single pixel detectors could be useful for deriving optical properties of samples, as the temporal profile of backscattered light shows significant dependence on the reduced scattering coefficient.

4.0 REFERENCES

1. Baribeau, R., W. S. Neil, and E. Cote (2009). “Development of a robot-based gonioreflectometer for spectral BRDF measurement”. In: *J. Mod. Opt.* 56(13), pp. 1497–1503 1.

2. Bashkatov, A. N. et al. (2005). “Optical properties of human skin, subcutaneous and mucous tissues in the wavelength range from 400 to 2000 nm”. In: *J. Phys. D: Appl. Phys.* 38(15), p. 2543 1.

3. Beek, J. F. et al. (1997). “In vitro double-integrating-sphere optical properties of tissues between 630 and 1064 nm”. In: *Physics in Medicine & Biology* 42, no. 11 4.

4. Bolin, F. P. et al. (1989). “Refractive index of some mammalian tissues”. In: *Appl. Opt.* 28(12), pp. 2297–2303 4.

5. Dam, J. S. et al. (2000). “Multiple polynomial regression method for determination of biomedical optical properties from integrating sphere measurements”. In: *Appl. Opt.* 39, pp. 1202–1209 1.

6. Debeer, S. et al. (2013). “Comparative histology and immunohistochemistry of porcine versus human skin”. In: *European Journal of Dermatology* 23, pp. 456–466 2, 5.

7. DeLisi, M. P. et al. (2019). “Optical properties of thermally damaged porcine dermis and subcutaneous fat.” In: *Proc. SPIE* 10876, 108760F 1, 10.

8. Edwards, D. K. et al. (1961). “Integrating Sphere for Imperfectly Diffuse Samples”. In: *J. Opt. Soc. Am.* 51(11), pp. 1279–1288 1.

9. Eggleston, Thomas A. et al. (2000). “Comparison of two porcine (Sus scrofa domestica) skin models for in vivo near-infrared laser exposure.” In: *Comp. Med.* 50(4), pp. 391–397 2, 5.

10. Farrell, T. J., M. S. Patterson, and B. Wilson (1992). “A diffusion theory model of spatially resolved, steady-state diffuse reflectance for the noninvasive determination of tissue optical properties in vivo”. In: *Med. Phys.* 19(4), pp. 879–888 1.

11. Ferrero, A. et al. (2013). “Spectral BRDF-based determination of proper measurement geometries to characterize color shift of special effect coatings”. In: *J. Opt. Soc. Am. A* 30, pp. 206–214 1.

12. Friebel, M. et al. (2006). “Determination of optical properties of human blood in the spectral range 250 to 1100 nm using Monte Carlo simulations with hematocrit-dependent effective scattering phase functions”. In: *J. Biomed. Opt.* 11(3), p. 034021 1.

13. Henyey, L.G. and J.L. Greenstein (1941). “Diffuse Radiation in the Galaxy”. In: *Astrophysical Journal* 93, p. 70 20.

14. Jacques, S. (1993). “Video reflectometry to specify optical properties of tissue in vivo”. In: *Proc. SPIE* 10311, p. 103110D 2.

15. Jacquez, J. A. and H. F. Kuppenheim (1955). “Theory of the Integrating Sphere”. In: *J. Opt. Soc. Am.* 45(6), pp. 460–470 1.

16. Jeught, S. Van der, J. A. Buytaert, and J. J. Dirckx (2012). “Real-time geometric lens distortion correction using a graphics processing unit”. In: *Opt. Eng.* 51(2), p. 027002 6.

17. Kienle, Alwin et al. (1996). “Spatially resolved absolute diffuse reflectance measurements for noninvasive determination of the optical scattering and absorption coefficients of biological tissue”. In: *Appl. Opt.* 35(13), pp. 2304–2314 2, 7.

18. Lanzafame, R. J. et al. (2014). “The growth of human scalp hair in females using visible red-light laser and LED sources in surgery and medicine”. In: *Lasers Surg. Med.* 46(8), pp. 601–607 1.

19. Li, H. et al. (2006). “Automated three-axis gonioreflectometer for computer graphics applications”. In: *Opt. Eng.* 45(4), p. 043605 1.

20. Liang J. Zhu, L. and L.V. Wang (2018). “Single-shot real-time femtosecond imaging of temporal focusing”. In: *Light: Science & Applications* 7, p. 42 1.

21. Ma, T. et al. (2018). “Noncontact evaluation of soluble solids content in apples by near-infrared hyperspectral imaging”. In: *J. Food Eng.* 224, pp. 53–61 2.

22. Mignon, C. et al. (2018). “Shedding light on the variability of optical skin properties: finding a path towards more accurate prediction of light propagation in human cutaneous compartments”. In: *Biomed. Opt. Express* 9(2), pp. 852–872 1.

23. Mihalas, D. (1978). *Stellar Atmospheres*. San Francisco: W. H. Freeman & Company 23.

24. Pfaff, S. et al. (2015). “Prospective randomized long-term study on the efficacy and safety of UV-free blue light for treating mild psoriasis vulgaris”. In: *Dermatology* 231(1), pp. 24–34 1.

25. Pickering, J. W. et al. (1992). “Two integrating spheres with an intervening scattering sample”. In: *J. Opt. Soc. Am. A* 9, pp. 621–631 1.

26. Pier, E.A. and J.H. Krolik (1992). “Infrared Spectra of Obscuring Dust Tori Around Active Galactic Nuclei I. Calculational Method and Basic Trends”. In: *Astrophysical Journal* 401, p. 99 23.

27. Prahl, S. A., M. J. C. van Gemert, and A. J. Welch (1993). “Determining the optical properties of turbid media by using the adding-doubling method”. In: *Appl. Opt.* 32(4), pp. 559–568 2, 4.

28. Qu, J. Y., Z. Huang, and Hua J. (2000). “Excitation-and-collection geometry insensitive fluorescence imaging of tissue-simulating turbid media”. In: *Appl. Opt.* 39, pp. 3344–3356 2.

29. Roggan, A. et al. (1994). “Determination of optical tissue properties with double integrating sphere technique and Monte Carlo simulations”. In: *Proc. SPIE* 2100, pp. 42–56 1.

30. Salomatina, E. et al. (2006). “Optical properties of normal and cancerous human skin in the visible and near-infrared spectral range”. In: *J. Biomed. Opt.* 11(6), pp. 64026–64029 1.

31. Schröder, S. et al. (2011). “Angle-resolved scattering: an effective method for characterizing thin-film coatings”. In: *Appl. Opt.* 50, pp. C164–C171 1.

32. Simpson, C. R. et al. (1998). “Near-infrared optical properties of ex vivo human skin and subcutaneous tissues measured using the Monte Carlo inversion technique”. In: *Phys. Med. Biol.* 43(9), p. 2465 1.

33. Sole, A. S., I. Farup, and S. Tominaga (2015). “An image-based multi-directional reflectance measurement setup for flexible objects”. In: *Proc. SPIE* 9398, 93980J 2.

34. Swarnakar, V. et al. (1997). “Integrated distortion correction and reconstruction technique for digital mosaic mammography”. In: *Proc. SPIE* 3031, pp. 673–681 6.

35. Vincelette, R. et al. (2012). *A Comparative Study of Melanin Content and Skin Morphology for Three Commonly Used Laboratory Swine (Sus scrofa domestica)*. Tech. rep. AFRL-RH-FS-TR-2013-0004. TASC INC San Antonio TX: Air Force Human Effectiveness Directorate Directed Energy Bioeffects Division Optical Radiation Branch 2, 5.

36. Vorburger, T. V. et al. (1984). “Surface roughness studies with DALLAS-detector array for laser light angular scattering”. In: *J. Res. Nat. Bur. Stand.* 89(1), pp. 3–16 2.

37. Wang, L., S. L. Jacques, and L. Zheng (1995). “MCML—Monte Carlo modeling of light transport in multi-layered tissues”. In: *Comput. Meth. Prog. Bio.* 47(2), pp. 131–146 1, 4.

38. Würth, C. and U. Resch-Genger (2015). “Determination of photoluminescence quantum yields of scattering media with an integrating sphere: direct and indirect illumination”. In: *Appl. Spectrosc.* 69(6), pp. 749–759 1.

39. Xia, Jinjun and Gang Yao (2007). “Angular distribution of diffuse reflectance in biological tissue”. In: *Appl. Opt.* 46(26), pp. 6552–6560 2.